

migration path. This path involves filling each shallow fault-dip trap to spill point towards the fault tips, with stratal migration forced around the outer flanks of the fault-related folds. Successive fill-to-spill leads to a continuous trail of amplitude anomalies that merge into a continuous, larger, gas-charged anomaly pattern. The migrating gas finally accumulates within a zone bounded by a large boundary fault with full juxtaposition seal. The pattern of anomaly distribution suggests that the hydrocarbon migration has been active in the Late Pleistocene and is probably continuing at the present day. Hence this plumbing system may be one of very few examples described to date in which dynamic hydrocarbon migration pathways have been directly imaged by seismic data.

Keywords

Hydrocarbon leakage, shallow gas, fluid flow, en-echelon faults, South China Sea

1. Introduction

Hydrocarbon plumbing systems in the shallow sections of petroliferous basins have been widely documented in the past two decades ([Roberts et al., 2000](#); [Heggland, 2004](#); [Berndt, 2005](#); [Cartwright et al. 2007](#); [Løseth et al. 2009](#); [Andresen, 2012](#); [Anka et al., 2012](#); [Ostanin et al., 2013](#)). They are often, but not exclusively associated with leakage from deeper-seated hydrocarbon reservoirs, and thus provide an important constraint on hydrocarbon prospectivity ([Judd & Judd, 2007](#); [Ostanin et al. 2017](#); [Foschi & Cartwright 2019](#); [Mohammedyasin et al., 2016](#)) as well as environmental risk (e.g. slope failure) ([Berndt et al., 2012](#); [Karstens and Berndt, 2015](#)). The detection of such plumbing system stems from increasing availability of high resolution 3D seismic surveys. The seismic data illuminates shallow gas through amplification and polarity changes (e.g. [Cartwright et al. 2007](#);

Judd & Hovland, 2007; Løseth et al. 2009). The passage of hydrocarbon gases such as methane often leaves a trail, in the form of stratal reflection disruption (e.g. enhanced reflectivity, phase reversals and bright spot) through scattering of energy by localized gas pockets, or by vertical soft sediment deformations (e.g. mud diapir, mud volcano and gas chimneys) (Heggland, 2004; Gay et al., 2007; Andresen, 2012). Finally, seafloor expulsion leaves recognizable traces through the formation of pockmarks and seafloor mounds (Roberts & Carney, 1997; Roberts et al., 2000; Judd & Hovland, 2007; Sun et al., 2011; Eruteya et al., 2018), or near seafloor methanogenesis (O'Brien & Woods, 1995; Ho et al., 2012; Feng et al., 2015).

Shallow plumbing systems generally consist of two main components (Andresen, 2012), vertical pathways (seal bypass systems of Cartwright et al. 2007), and stratal storage or migration pathways. In many petroleum basins, faults offer the best potential vertical migration routes but the same faults are also required to form lateral barriers to migration in order for reservoirs to form valid traps. This duality of fault behavior was discussed (e.g. Yielding et al., 1997; Ligtenberg, 2005; Cartwright et al., 2007; Jackson & Rotevatn, 2013; Edmundson et al., 2019), and a suggested explanation was that vertical leakage could be transient, and restricted to periods of active faulting, whereas static lateral sealing would be the norm for dormant period of fault activity. Previous studies have typically focused on either the vertical fluid migration (e.g. Cartwright et al. 2007; Løseth et al. 2009) or the lateral fluid migration (e.g. Bünz et al., 2003; Berndt et al., 2004). The interplay of vertical and lateral migration has received much less attention in comparison (Cowley & O'Brien, 2000; Andresen, 2012). These studies often share a common approach of documenting fluid flow indicators or direct hydrocarbon indicators and building those combined observations into a reconstruction of the hydrocarbon plumbing system (Andresen, 2012). Direct observations of active

hydrocarbon migration pathways are extremely rare, and to date have been limited to hydrocarbon movements related to production or drilling. An excellent example of this type of study is [Landro et al. \(2019\)](#), who used active and passive seismic methods to track gas migration that resulted from a blow out during drilling operations.

Here we describe a shallow hydrocarbon plumbing system from the South China Sea, where we interpret amplitude anomalies mapped on a 3D seismic dataset and argue that the patterns exhibited by these anomalies are indicative of currently active (dynamic) hydrocarbon migration, exploiting a combination of stratal and cross-stratal pathways. We use standard 3D seismic interpretational techniques and calibration with one exploration borehole to document the migration pathways with respect to the trapped hydrocarbon distribution. In particular, we use the amplitude maps of key horizons to demonstrate the interplay between vertical and stratal migration, and we interpret active fill-and-spill processes related to the predominant fault-dip trap configuration.

Dynamic migration processes are usually inferred from pressure differences ([Hubbert, 1953](#); [Dahlberg, 1995](#)), but to our knowledge, direct evidence for natural as opposed to anthropogenic, dynamic hydrocarbon migration (hydrocarbons in transit) has not previously been inferred from simple mapping of borehole calibrated, seismic amplitude anomalies. The aim of this paper is therefore to draw attention to the potential to use 3D seismic to detect batches of hydrocarbons in transit, as opposed to statically trapped in a fixed position. The interpretation of amplitude anomalies and other direct hydrocarbon indicators does certainly carry some uncertainty, but a secondary aim here is to show how an analysis of the planform of those amplitude anomalies can help reduce this uncertainty, and firm up an interpretation of the presence of hydrocarbons. Our study was calibrated by exploration boreholes, but we think this approach could be useful for areas without any direct

calibration from drilling results.

2. Geological setting

The study area is located within the Pearl River Mouth Basin (PRMB), one of several rift basins of Late Cenozoic age in the northern continental margin of the South China Sea. The PRMB covers an area of ~175,000 km² with length of ~750 km and width of ~300 km (Fig. 1). The basin is mainly subdivided into several northeast-southwest extended ‘sags’ (intra-basinal grabens/half-grabens) and ‘massifs’ (intra-basinal horsts) (Fig. 1a). Our study area with present water depths ranging from ~180 m to ~310 m is located in the eastern part of the Panyu Low Massif (Fig. 1a). The Panyu Low Massif is bounded by the half-graben of the Baiyun Sag to the south that is the main locus for hydrocarbon generation for all the hydrocarbon fields in the surrounding area (Pang et al., 2007), and by the intra-basinal horst of the Dongsha Massif to the east and north (Fig. 1a).

The PRMB experienced a Late Cretaceous - Early Oligocene rifting stage, a Late Oligocene–Early Miocene transitional stage and a thermal subsidence stage since the Middle Miocene (e.g. Ru & Pigott, 1986; Yu, 1994; Gong & Li, 1997). This period of basin development was punctuated by three main tectonic events, namely, the Zhuqiong Event, the Nanhai Event and the Dongsha Event (e.g. Pang et al., 2008; Dong et al., 2009) (Fig. 2). These events involved major tectonic activity often localized along boundary faults separating intra-basinal grabens and horsts (Fig. 1a). The three episodes of active faulting are dated as 32-29 Ma, 23.8-21 Ma and 18.5-16.5 Ma (Deng et al., 2019), and deformed both the syn-rift and transitional successions. The Dongsha Event has involved uplift and faulting around the Dongsha Massif (Fig. 1a) since ~10.5 Ma (Lüdmann & Wong, 1999). Moreover, this neotectonic event was associated with dextral shear of the study area (the Panyu Low

Massif) and en-echelon faulting (Zhang et al., 2010).

Periods of active faulting in the PRMB have been dated using seismic-stratigraphy and borehole data, and in the study area the main phases of faulting likely ceased prior to ~3.0 Ma (Gong & Li, 2004; Wang, 2007). Towards to the Dongsha Massif, faults were active for a longer period and some are presently active in the Dongsha Massif (Wang, 2007), where some of the boundary faults offset the seabed (Sun et al., 2014a).

The Baiyun Sag (Fig. 1a) was infilled by a total sediment thickness of >10 km (Pang et al., 2008), with the sedimentary environment changing from fluvial-lacustrine in the early stage (>23.8 Ma) to shallow, marginal marine (embayment), and finally to open marine (hemipelagic) in the late stage (from 23.8 Ma to Present) (Zhu et al., 2009). Syn-rift non-marine mudstones and coals (pre-Late Oligocene; Wenchang and Enping Formations) represent the main hydrocarbon source rocks within the region (Huang et al., 2003) (Fig. 2). During the syn-to-post rift transition (Late Oligocene-Early Miocene), marginal marine sandstones were deposited (Zhu et al., 2009). These sandstones are extensively distributed and serve both as regional hydrocarbon reservoir units and carrier beds (Shi et al., 2009) (Fig. 2). These reservoir-like facies were overlain by thick fine-grained sediments with thin siltstone layers in the Baiyun Sag and Panyu Low Massif (Huang et al., 2003).

Faulting related to the Dongsha Event has been argued to provide the main vertical pathways for secondary hydrocarbon migration from the source rocks (e.g. Pang et al., 2008; Chen et al., 2013); whilst the extensive sandstones (23.8-18.5 Ma and 16.5-13.8 Ma) acted as carrier beds from the Baiyun Sag to the Panyu Low Massif (the study area) (e.g. Pang et al., 2007; Shi et al., 2008; He et al., 2009). Importantly, the hydrocarbons mainly migrated along a structural ridge from the Baiyun Sag northeastwards to the Panyu Low Massif (Fig. 1b; Zhu et al., 2006; Shi et al., 2009; Ping et al.,

2019), and several fault-controlled gas fields formed along this migration route (e.g. Wang, 2007; Zhu et al., 2005) (Fig. 1b). Moreover, the northeasterly hydrocarbon charging become younger more distally away from the Baiyun Sag (Fig. 1b; Zhu et al., 2006). Hydrocarbon charge into the sandstone reservoir (Zhujiang Formation) in our study area is inferred to have occurred over the period ~2.7-0.6 Ma using organic geochemical and fluid inclusion data (Ping et al., 2019) (Fig. 2).

3. Data and Methods

This study is mainly based on a post-stack, time-migrated 3D seismic survey that covers an area of ~1350 km² (Fig. 1a). The data were acquired and processed by the China National Offshore Oil Corporation (CNOOC). It is processed using a standard sequence for marine seismic data (deconvolution, dynamic/static correlation, digital filtering, multiple suppression, offset stack and post-stack migration), and finalized to zero phase and normal polarity (downward increase in acoustic impedance corresponding to a positive reflection event; e.g., Brown, 2004). The bin size of this 3D seismic survey is 12.5 × 25 m and the vertical sample rate is 2 ms. Therefore, the lateral resolutions are 12.5 m in inline (N-S) and 25.0 m in crossline (E-W). The dominant frequency of the interval of interest is ~45 Hz. This frequency, using a p-wave velocity of ~2000 m/s (based on the exploration well N119-5-3) yields a vertical resolution of ~11 m.

Root mean square (RMS) and variance slices from a variance volume, were used to constrain the distributions and characteristics of seismic anomalies and normal faults. The RMS attribute measures the reflectivity of a given time window (thickness) of seismic data and it computes the square root of the sum of squared amplitudes, divided by the number of samples within the specified window used (Brown, 2004). The RMS attribute could clearly image variable amplitude anomalies

in seismic data, such as free gas and sedimentary facies change (Chopra & Marfurt, 2007; Karfurt & Alves, 2015), which would help to delineate the distribution of free gas in this study. In this study, a root-mean square amplitude (RMS) attribute map calculated in a window from 700 to 900 ms TWT are used to illustrate the distribution of high-amplitude seismic amplitude anomalies (AAs) in the shallow level. The variance attribute measures the variability in shape between seismic traces, which could be done in a specified window along a picked horizon or within a full 3D seismic volume. The variance attribute is typically invaluable when mapping structural and stratigraphic discontinuities, such as faults and channels (Brown, 2004; Karfurt & Alves, 2015).

Seismic stratigraphic units (Fig. 2) were correlated to those classified by the CNOOC and documented in previous studies (e.g. Pang et al., 2007; Shi et al., 2009; Zhu et al., 2009), and were also calibrated by the exploration well N119-5-3 (Fig. 3). The exploration well N119-5-3 was drilled through the Quaternary - early Miocene strata and terminated at depth of 2611 m below sea floor (mbsf) with age of ~23.8 Ma. This well was also used for correlations of lithology, gas content and strata velocity.

The T-z measurements using the method by Cartwright et al. (1998) are displayed as individual plots of a single profile transect. The normal faults in Group II (see details in Section 4.3) that terminate in different levels and have different inclinations are selected for the T-z measurements.

4. Results

4.1. Seismic Stratigraphy

Four seismic units, Unit 1 – Unit 4 from old to young, are subdivided in this study, based on the seismic facies and configurations (Fig. 3).

Unit 1 is bounded by surface T₄ as its top which is a strong, continuous, positive seismic reflector (Figs. 3, 6). In the upper part of Unit 1, it is characterized by high-amplitude, continuous and parallel seismic reflections. In its lower part, the high-amplitude, continuous seismic reflections onlapped onto the basement highs (Fig. 6). These seismic configurations result in a variable thickness of Unit 1 that gradually thins towards to the basement highs. The basement is mainly composed of early Cretaceous granite (Liu et al., 2018). At the base of Unit 1 where the strata was drilled by well N119-5-3 (below surface T₄ of ~18.5 Ma), it is composed of ~50 m thick sandstone (medium sand; GBL1 in Fig. 3) that is interpreted as delta plain facies and serves as the main hydrocarbon reservoir in the study area (e.g. Pang et al., 2007; Wang et al., 2012; He et al., 2017) (Fig. 3). Moreover, free-phase gas is identified within this deep reservoir (e.g. Pang et al., 2007). Normal faults are frequently observed within Unit 1.

Unit 2 is bounded between surfaces T₄ and T₂ (Fig. 3). It is mainly characterized by moderate-amplitude, continuous, parallel seismic reflections (Figs. 3, 6-7). Unit 2 is dominated by mudstone interbedded with sandstone and siltstone beds (Fig. 3). Furthermore, well N119-5-3 shows that there are three sandstone-dominated layers within Unit 2 and they are close to the positions of seismic surfaces T₃ (~13.8 Ma; 20 m thick; GBL3 in Fig. 3), T₃ (~14.3 Ma; 29 m thick) and T₃₁ (~15.5 Ma; 18 m thick; GBL2 in Fig. 3). Free-phase gas is identified in the sandstones around surface T₃ (e.g. Pang et al., 2007). Unit 2 is also frequently crosscut by normal faults. In addition to the faults that extended from Unit 1, there are also many secondary faults occurring within Unit 2 (Fig. 7).

Unit 3 is bounded by surfaces T₂ and T₁, has moderate-weak, continuous, parallel-subparallel seismic reflections (Fig. 3). Unit 3 is crosscut by the normal faults that are present in unit 2 and unit 1. The lithology of Unit 3 is dominated by mudstone interbedded with argillaceous siltstone beds.

These argillaceous siltstone layers with variable thicknesses are shelf facies (Fig. 3). There are many high-amplitude seismic amplitude anomalies (AAs; for details see section 4.3.2) occurring within this unit (Figs. 3, 7). Amongst them, two pronounced high amplitude anomalies encountered in well N119-5-3 correspond precisely to two argillaceous siltstone layers each about 10 m thick (786.3-796.5 mbsf of GBL5 in Fig. 3 and 798.4-808.9 mbsf of GBL4 in Fig. 3) (See section 4.3.2). Importantly, free-phase gas is identified in these two siltstone layers from mud log data and drilling reports (e.g. Pang et al., 2007). The free gas in these two layers and deep reservoir level (around surfaces T₃ and T₄) is thermogenic in origin (delta C₁₃ values of -25 - -55‰, C₁/(C₂ + C₃) of 45-65). The gas-charged sandstones/siltstones layers generally have low gamma-ray (GR) and high sonic values (DT) (Fig. 3).

Unit 4 is between surface T₁ and seabed, which is mainly characterized by weak-amplitude seismic reflections (Fig. 3). High-amplitude seismic reflections are also locally observed. It is subdivided into two parts by surface T₀, a regional unconformity with a continuous, high-amplitude seismic reflection (Fig. 3). The lower part consists of sub-parallel seismic reflections that are eroded by surface T₀. Whilst the upper part shows progradational clinoforms and downlap onto surface T₀ (Fig. 3). Faults are rarely observed within Unit 4. Only the lowermost part of Unit 4 is drilled by well N119-5-3, showing that the lithology of Unit 4 is dominated by mudstone interbedded with argillaceous siltstone beds (Fig. 3).

4.2. Generalised structure and seismic character of the study area

The overall sedimentary package within the study area is characterized by a gentle SW dip of about 0.3° measuring from seismic section in the shallow level (Fig. 8). The strata are extensively

deformed by a normal fault system that form a striking en echelon planform geometry and apparently extensional displacements (Figs. 4-8). Shallow basement is observed below the deep-seated reservoirs (around surface T₄) and the positive structural influence of this basement feature persists upwards above surface T₃ (Fig. 6). The shallow basement structure may comprise part of the structural ridge that promotes the northeastward migration of hydrocarbons in the Panyu Low Massif (Fig. 1b; e.g. Pang et al., 2008; Shi et al., 2008, 2009).

The north of the study area is dominated by a large basement-rooted normal fault, referred to here as the Panyu Fault (Fig. 9). The Panyu Fault has an along-strike length of a minimum of 45 km and extends vertically from the basement to the seabed, with a maximum throw of >1 km at the top of basement. All the other faults observed in the study area are considerably smaller in throw and length than the Panyu Fault, and occur as isolated structures or within the en-echelon arrays (Fig. 5). Most of these faults are less than 10 km long and are characterized by modest dips of ~40-45° (Figs. 5, 10).

AAs and several vertical zones of almost complete seismic stratal disruption are observed in the study area. The AAs are located within Unit 3 between surfaces T₁₁ (~8.5 Ma) and T₁ (~5.5 Ma) (Fig. 3). They occur in both singular entities (one seismically amplified reflector) or stacked (several closely spaced seismic reflectors). They vary considerably in planform geometry and dimensions (areal extents ranging from 1 km² to ~200 km²). The vast majority of the encountered AAs (>96 %) occur south of the E-W boundary fault and crudely cluster into three connected groups (Zone A, B and C in Fig. 5) oriented approximately E-W and located at the center of the study area.

4.3. Detailed seismic observations

4.3.1. Faults

The largest fault in the area is the Panyu Fault separating the Panyu Low Massif from the Dongsha Massif to the north (Figs. 1a, 9). It penetrates the entire basin fill up to the seabed where there is a visible fault scarp of ~10 m relief (Fig. 9). There is localized drag folding against the sharp cut-offs at the fault plane. The footwall is relatively flat lying, but geometries are obscured close to the fault plane by the fault shadow zone effect, and by local attenuation/disruption relating to the AAs (Figs. 9, 11).

To the south of boundary fault (Panyu Fault), 95 minor faults with normal throws of 10s TWT are identified by the variance slices and seismic profiles (Figs. 4-11). Individually they are linear or gently curvilinear in plan. These apparently normal faults dip both to the NE (20°-50°) and the SW (210°-240°; Fig. 10b), and have a main strike of NW-SE (290°-325°) (Fig. 10a). The strike lengths of these faults range from ~0.7 km to ~13.2 km (Fig. 10c) with an average of ~3.0 km in the focused strata of this study where AAs occur (~700-900 ms twt). These faults usually terminate upwards with upper tips clustering close to surface T₁ (~5.5 Ma) (Fig. 3). They extend downwards to the basement with minor offset of the deeper horizons and no evidence of detachment (Figs. 3, 7). The sandstone reservoir (near surface T₄) is frequently transected by these faults (Fig. 3).

The vertical variation of throw on these minor faults was established by constructing a set of throw versus 'depth' plots. These T-z plots exhibit C (e.g. F7 and F8) and M (e.g. F2 and F3) patterns (Fig. 10d) (Muraoka & Kamata, 1983), but with quite steep throw gradients near the upper tips similar to small syn-sedimentary normal faults as documented in the Levant Basin (Baudon & Cartwright, 2008a, b), Egersund Basin (Tvedt et al., 2013) and Hammerfest Basin (Omosanya et al., 2015).

The distribution of minor faults in the study area is dominated by two ENE trending arrays of en-echelon faults (Group I and Group II; Fig. 4). The variance slices also show that the normal faults probably extend into the chaotic seismic zones indicated by the dark seismic zones in Figure 4b (see section 4.4.4 for details). Individual faults in these two en echelon groups are curvilinear, with weakly sinuous traces, typically striking NW-SE, mainly dipping NE and with typical strike length ranging between 3 km and 7 km (Figs. 4b, 10a-c). These en echelon arrays are seemly linked to the deep-seated structures in the basement (Fig. 4d) and interpreted as the product of an oblique extensional reactivation of a basement structure at depth, similar to that obtained in analogue models of oblique extension (McClay & White, 1995; Clifton et al. 2000). The apparently normal throws observed on individual faults could be expected to have a true oblique slip vector, and this in turn would affect their along plane transmissibility (Lefèvre et al., 2016). The combination of en echelon faults and basement relief led to the development of a number of fault-dip traps for reservoirs at deeper levels (early Miocene sandstone; surface T₄ - surface T₃) (Figs. 12a-b). The structurally shallowest points of the fault-dip closures in the footwalls are immediately adjacent to the fault planes (Fig. 12a).

4.3.2. Amplitude anomalies (AAs) and relationship to faults

The AAs (Figs. 3, 5a-b) are characterized by a strong amplification of the generally low to moderate background seismic reflectivity and are sharply defined by abrupt lateral amplitude cut-offs (Figs. 6-7, 11). The reflection amplification occurs preferentially on the soft loop of the Ricker-like zero-phase wavelet, and is best observed on isolated reflections with sufficient vertical separation from other amplified reflections. Closely spaced, vertically stacked AAs are also

observed mainly on the footwall strata (Fig. 9). These stacked AAs are consistent with previously documented examples of vertically stacked, gas-related DHIs termed vertical anomaly clusters that have been interpreted as evidence of focused vertical gas migration (Ostanin et al., 2013; Foschi et al., 2014; Mohammedyasin et al., 2016; Bertoni et al. 2018).

The AAs are best developed in the south-central part of the study area (Fig. 5), within the shallow stratigraphic interval between T₁ and T₁₁ (Fig. 3). A prominent set of anomalies form above the basement high, where there are several large stacked anomalies apparently feeding smaller groups of anomalies at shallower levels (Fig. 6).

The majority of AAs are closely associated with the minor faults (Fig. 7), and also the Panyu Fault (Fig. 9). These fault-bounded anomalies usually distributed vertically along fault planes over the entire supra-reservoir interval (e.g. Fig. 9). A number of faults have no AAs associated with them whatsoever, especially those occurring outside the en echelon fault zones (Fig. 8).

The RMS attribute map extracted in a window from 700 to 900 ms TWT shows that the AAs are distributed into three concatenated zones oriented approximately E-W (Fig. 5). These zones are closely associated with the fault groups (Fig. 5b) as follow from south to north: Zone A is related to Group I, Zone B is related to Group II, and Zone C is related to Group II and the Panyu Fault (Fig. 5b). The fault/dip closure of the main gas field in the area (e.g. Pang et al., 2007; Wang et al., 2012; Fig. 12a) is located in the deep level (Unit 1) (Fig. 3) of the westernmost part of Zone A (Fig. 5b).

In Zone A and Zone B, the RMS amplitude pattern is strongly influenced by the fault pattern shown by continuous but irregular gross planforms with a NW-SE orientation (Fig. 5). These linear high amplitude zones are delimited by the footwalls of the two en echelon arrays in Zone A and B. Low amplitudes close to the fault plane are positioned in the hangingwalls (Fig. 5). Importantly, the

high RMS zones form a continuous swathe along the south-eastern tips of the faults in both arrays, created a serrated but uniform zone of the high AAs along the southeastern margins, which is most evident at the easternmost part of Zone B (Fig. 5b). In Zone C, the high RMS amplitude is also strictly limited by the northern tips of southwest-dipping faults (Group II) to the south and by north-dipping boundary fault to the north (Figs. 5, 9). Some AAs are located close to the seabed along the boundary fault (Fig. 11).

4.3.3. Vertical seismic anomalies

Vertical anomalies characterized by chaotic seismic reflectivity are observed in association with AAs across the study area (Fig. 11). A large seismic chaotic zone (SCZ-1) occurs at the southwestern part of the study area (Figs. 5b, 11). This SCZ-1 anomaly extends vertically from the deep level and abuts against a group of the AAs in the shallow strata, before dying out at or close to the modern seabed. The base of this anomalous zone is hard to define because of scattering and attenuation artefacts, however the chaotic seismic reflections seem to root close to the deeper reservoir level in the footwall of a c. 50 m (50 ms twt) throw fault (Figs. 11a-b). At its upper limit, this vertical anomaly crosses the AAs and terminates with an acoustic bright anomaly characterized by a hard polarity (Fig. 11). The AAs are clearly offset and are not located in the same stratigraphic level (Figs. 11a-b). The reflection package from below the bright hard patch to about 1.7 ms TWT is characterized by a 'pull-up' or mounded geometry where the reflections steepen towards the center of the chaotic zone (Figs. 11a-b). Above the bright hard patch, some AAs are observed within 100 m or so of the seabed (Fig. 11). The recent development of this vertical seismic anomaly is evidenced by a mounded structure on the seabed with a height of ~10 m (Fig. 13a) and high RMS amplitude

(Fig. 13b).

Several other vertical seismic chaotic zones are observed in the study area (SCZ-2, 3, 4 and 5) that have similar seismic characteristics to anomaly SCZ-1 (Figs. 6, 11c-d). However, SCZs 2-5 are narrower and located within footwalls close to normal faults. Moreover, these normal faults penetrate upwards to the hard seismic reflections identified within the chaotic zones (Figs. 11c-d). Similarly to SCZ-1, the bases of SCZs 2-5 (*sensu* Moss & Cartwright, 2010) are difficult to locate because of artefact trails. Nearer to the surface, narrow, ‘pipe-like’ zones with small-scale AAs close to the seabed are also observed above the hard seismic reflections (Fig. 11). Importantly, the vertical chaotic zones do not appear to root from the shallowest point of any closures at the deeper reservoir level (Figs. 11, 12a).

5. Discussion

5.1. Possible origins for the studied amplitude anomalies (AAs)

Seismic AAs as documented in this study can be caused by lithological effects, seismic tuning of thin layers, and gas charging sediments. Local amplitude variations due to lithological effects are easily excluded from this interpretation, because they result in only modest amplitude variation, an order of magnitude lower than the threshold for the AAs (Judd & Hovland, 2007; Calvès et al., 2008). The AAs (e.g. the two gas-bearing layers GBL4 and GBL5 in Fig. 3) are ~10 m thick, which is similar to the tuning thickness (~11 m; quarter of wavelength; Sheriff, 2002). The amplification of the seismic response (amplitude) expressed by AAs and specifically the variation of seismic response from “soft” to “softer” is typical for shallow gas-charged soft sediments (Rutherford, 1975;

Judd & Hovland, 2007; Løseth et al., 2009). Reflections directly beneath the AAs (Figs. 6, 11) exhibit signs of frequency attenuation classically associated with the presence of free gas (Castagna, 1994). These diagnostic geophysical observations combined with the direct calibration of some of the AAs in well N119-5-1 as being due to hydrocarbon gas substitution of pore water in thin reservoir sands or silts (Fig. 3), indicates that the AAs mapped throughout the study area result from the presence of hydrocarbon gases rather than seismic tuning. The widespread free gas accumulations typified by the AAs in our study area have not been reported previously. Here, we discuss the possible origins and migration pathways for these free gas accumulations.

5.1.1. Possibility of long-distance fluid migration

Hydrocarbon migration at the deeper level (below surface T_2) of the Panyu Low Massif and the Baiyun Sag has been discussed by many previous studies (e.g. Pang et al., 2008; Shi et al., 2008, 2009). Hydrocarbons sourced from the Baiyun Sag (Wenchang Formation and Enping Formation; e.g. Ping et al., 2018) flowed along the regional sandstone carrier beds (e.g. those of around surfaces T_3 , T_{31} and T_4) to the study area (e.g. Wang, 2007). Therefore, several gas fields are observed in the fault-controlled closures in the NE-extended play fairway of hydrocarbon migration (e.g. Shi et al., 2009; Ping et al., 2019).

We consider the possibility that the shallow gas occurrences were fed primarily via long-distance, lateral migration using carrier layers in Unit 3 from the Baiyun Sag to the study area (Fig. 14a). This model would be similar to the proven long-distance migration of the hydrocarbons in the deeper reservoirs (near surface T_4). However, lateral migration within the most permeable layers of Unit 3 would likely be limited by rapid lateral facies changes within the dominantly fine-grained sediments

of this interval. Potential carrier beds are the porous siltstones (e.g. the two siltstone layers with free gas; Fig. 3), but they are thin (~1 - 20 m) and only locally distributed because the study area was far from the sediment sources (Pearl River) (e.g. Wang et al., 2012; He et al., 2017). This contrasts with the more laterally extensive depositional environment of deep-level reservoirs of Unit 1 that were fed by the paleo-Pearl River Delta (e.g. Pang et al., 2007). An additional factor limiting lateral migration in the shallow strata (Unit 3) is the fault compartmentalization (e.g. Yu et al., 2007; Shi et al., 2009), which would have broken the continuity of any carrier beds acting as baffles or barriers to lateral migration.

An important regional constraint is that within the whole region, shallow gas in Unit 3 is only observed in a much localized area (study area) of the Panyu Low Massif (e.g. Pang et al., 2007). If longer range migration at the shallow level was the origin, we would have expected a much wider distribution of shallow gas accumulation. This limited distribution therefore indicates that the shallow gas likely has a local origin, e.g., from the deep gas reservoirs close to surface T₄ and/or gas-charged structures of surfaces T₃ and T₃₁) (Figs. 14b-c) or from the local accumulation of biogenic gas. The shallow gas from the two thin siltstone layers showing that its delta C₁₃ values is of -25 - -55‰ and C₁/(C₂ + C₃) is of 45-65, suggests it has a thermogenic, rather than biogenic origin (Zhu et al., 2009). Therefore, the local origins of vertical migration from deep levels are the most probable candidates which are detailedly discussed below.

5.1.2. Vertical migration origins through seismic chaotic zones vs normal faults

Based on our seismic observations, and having rejected long-distance lateral (stratal) migration, we infer that there are two possible pathways for vertical hydrocarbon migration from deep-seated

reservoir/gas-bearing layers (Unit 1 and Unit 2) to the shallow strata (Unit 3) (Figs. 14b-c). One is via the normal faults that intersect or delimit the fault-dip closures of the deep-level reservoirs (Figs. 11a-b, 12a, 14c); the other is via the hydraulic fractures/damage zones that are shown as vertical SCZs (Figs. 11, 14b).

5.1.2.1. Possibility of fluid migration through seismic chaotic zones

The origin of the vertical SCZs is critical to a discussion of potential cross-stratal migration pathways in the study area. Features such as SCZ-1 (Fig. 6) are typically interpreted as gas chimneys in many petroliferous basins based on their disrupted seismic character, association with amplitude anomalies, and vertical geometry (Heggland, 1997, 2014). If these SCZs (Fig. 11) are gas chimneys as we suspect, then they may have significantly contributed to the vertical gas migration from the deep-seated reservoirs to the shallow siltstones of Unit 3 (Figs. 11, 14b). However, the observation that the SCZs are not located at crestal points of the four-way closures (Figs. 11, 12a) is difficult to explain in this context, since gas chimneys most commonly form by crestal leakage (at the crest of reservoir) (Heggland, 2014). It is possible that weak points in the seal may serve as loci for upwards migration from the deeper reservoirs, similar to that invoked recently for the Scarborough Gas Field (Foschi & Cartwright, 2020), but we cannot evaluate this possible explanation at present.

The interpretation of the SCZs as gas chimneys is also made more problematic by transmission and velocity artefacts generated by the structures with high, positive impedance contrasts immediately above the disrupted zones (Fig. 11; Judd & Hovland, 2007). Shallow hard anomalies that are possibly carbonate cementation are well known to cause seismic disruption below (e.g. Hovland et al., 1994).

419

420 **5.1.2.2. Normal faults and their roles in vertical gas migration**

421 It is widely appreciated that normal faults may serve as either conduits for or barriers to fluid
422 flow (e.g. [Yielding et al., 1997](#); [Ligtenberg, 2005](#); [Jackson & Rotevatn, 2013](#)). The normal faults
423 generally transect the SCZs and terminate at the hard seismic anomalies (Fig. 4; [Fig. 11](#)), suggesting
424 perhaps that fluids flowing along the faults formed the hard anomalies at the upper fault tips. The
425 close spatial association between the SCZs and fault footwalls makes it uncertain whether both
426 function independently of each other.

427 Previous studies have argued that fault 'flags' i.e. amplitude anomalies abutting the fault plane
428 within footwall and hangingwall are strong evidence for along-fault vertical migration ([Traynor &
429 Sladen, 1997](#); [Løseth et al., 2009](#)). The observation of similar fault flags in the study area ([Fig. 7](#))
430 on a number of faults within the zone of generally elevated amplitudes (the main migration 'spillway'
431 ([Figs. 4, 9](#)) therefore increases the likelihood of some vertical transmission of gas along the fault
432 planes. Gas column height within the deep fault/dip closures is typically less than 100 m (well N119-
433 5-1) ([Fig. 12a](#)), which is unlikely to have promoted dilatancy on the faults by buoyancy alone
434 ([Mourgues & Cobbold, 2003](#)). Hence, for the faults to act as valves for the deep gas requires an
435 additional source of overpressure ([Mourgues & Cobbold, 2003](#)), or dilatancy induced during
436 episodes of active slip ([Cartwright et al. 2007](#)). Since pre-existing faults are mechanically weaker
437 than the undeformed host rocks (e.g. [Aydin, 2000](#); [Jourde et al., 2003](#)), it seems likely that any
438 significantly overpressured fluids would prefer to use pressure-dilated pathways up the normal
439 faults rather than to form new fracture networks in footwalls that form loci for gas chimney
440 development ([Cartwright et al. 2007](#)).

Further observations complicate this discussion:

(1) we note that not all the deep-rooted normal faults that intersect the main reservoir (close to surface T₄) are associated with shallow gas anomalies, and those lying outside the main amplitude anomaly zone (the ‘spillway’) are completely devoid of any gas indicators (Figs. 5, 7-8).

(2) Within the main ‘spillway’, the ‘fill-to-spill’ pattern along the footwalls of these faults (Figs. 5, 7), suggests that the normal faults mainly act as lateral barriers to the fluid flows in the study area at least in the recent past.

(3) The termination levels (around surface T₁; Fig. 3) of en-echelon normal faults together with their throw patterns showing in the T-z map (Fig. 10d) indicate that the main activity of normal faults ceased around 5.5 Ma (surface T₁), which agrees with the previous studies that the normal faults emplaced pre-3.0 Ma in the Panyu Low Massif (e.g. Wang, 2007). Therefore, the period of main gas charged of the deeper reservoirs (~2.7-0.6 Ma; Ping et al., 2019) post-dates the main activity of normal faults.

On balance, we suggest that both modes (normal fault pathway and gas chimney) of vertical migration have probably operated, but their length and time scales of activity are highly uncertain (Fig. 15). It may be that localized activity occurred during the main period of gas charge into the deeper reservoirs, since the activity on the major Panyu Fault clearly persist to the present day. Intermittently, low slip displacement of the fault network in a generally transtensive regime (as suggested by the en echelon fault patterns) may have led to transient tectonic dilatancy. Gas surge events during the main charge phase (sensu Sales, 1997) could have promoted the initial

development of gas chimneys (along the damage zone of faults or above the foci of four-way closures) that developed further by slow flux processed during fault dormancy. When dormant, the faults act as efficient lateral seals for the Unit 3 siltstones, and lead to the classic fill-spill patterns seen in the shallow amplitude map (Fig. 5).

The shallow plumbing system shown schematically in Figure 15 thus captures the spatial and temporal interplay between lateral and vertical gas migration as follows: (1) gas from the Baiyun Sag laterally migrated and charged the deep reservoirs (Fig. 15a); (2) gas of localized bleed-off from these deep reservoirs vertically migrated along faults with minor displacements or along footwalls hosted fracture networks indicated by gas chimneys (Fig. 15a); (3) the leaked gas injected into the shallow siltstones of Unit 3, and then (4) laterally migrated via a fault mediated fill and spill pathway updip along the main structural ridge (Fig. 15a). The leaked gas would steer by the ports of strata where the siltstone was completely offset by normal faults (Figs. 15b-c), which form the special fill-spill pattern as observed in Figure 5. Fluid flux related to plumbing system probably varied over time, depending on fault activity and pressure build up in key storage units. The specific amplitude pattern revealed in the Figure 5 is perhaps the first time that such a dynamic, fault mediated fill-spill system has been captured on seismic data, and strongly suggests that gas migration is active today.

5.3. Implications for dynamic accumulation and long-lived leakage of hydrocarbon in the SCS

The source kitchen in the Baiyun Sag is in the gas generative window at present (e.g. Zhu et al., 2005; Sun et al., 2012; Ping et al., 2019), which strongly supports previous suggestions that the long-distance hydrocarbon migration from the Baiyun Sag to the study area along the deep-level reservoir units is active today (e.g. Shi et al., 2009). This would promote a dynamic hydrocarbon

accumulation in the deep-level reservoir and long-lived, persistent hydrocarbon leakage along the faults. The high RMS anomalies and mounded structure at present seabed (Fig. 13), free gas along the boundary fault (Fig. 9) and gas chimney close to the seabed (Figs. 6b-c, 11) all collectively suggest that the hydrocarbon leakage is ongoing at present.

There are some risks for the hydrocarbon exploration in the deep-level reservoir, because the accumulated hydrocarbons may have been depleted by the long-lived, active hydrocarbon leakage. The leaked hydrocarbons have at least partially accumulated in the shallow reservoirs of Unit 3 and potentially form commercial accumulations of hydrocarbon, although previously ignored or have not yet been drilled. Moreover, the free gas in the shallow strata may also represent geohazards (e.g. Eruteya et al., 2015), which should be considered during drilling design.

6. Conclusions

High-resolution 3D seismic data and one exploration well are used to characterize the structures (normal faults and basement highs) and seismic anomalies (AAs and seismic chaotic zone) in this study. Five main conclusions can be drawn from this study.

1. Two types of seismic anomalies, AAs and seismic chaotic zone, are observed in this study and they are interpreted as free gas and gas chimney, respectively;
2. Two groups of en-echelon faults (normal faults) occurred in the study area and mainly serve as barriers to the fluid flow. They caused the AAs to distribute as a fill-spill pattern in plan view.
3. Some en-echelon faults that formed the four-way closures in the deep levels are likely to be critically stressed, because of the mechanical weak zone of these faults and the high gas columns (pressure) within the four-way closures. Hydrocarbon leaking from deep-seated reservoir (four-

way closures) could migrate upward along these faults. Gas chimney maybe also partly contribute to the vertical migration of hydrocarbon;

4. Most of the leaked gas charged the porous siltstone in the shallow level from which the leaked gas laterally migrated updip within the strata. Some of the leaked gas continuously migrated upward and reached present seabed;

5. This study presents evidence for the vertical and lateral pathways of a long-lived, ongoing hydrocarbon leakage (a dynamic hydrocarbon migration/accumulation process). Considering the structures (e.g. normal fault and gas chimney) observed in this study are widespread in the continental basins (e.g. the Levant Basin and Lower Congo Basin), the approach taken in this study can probably be applied to other petroliferous basins.

Acknowledgements

This work was supported by the National Scientific Foundation of China (Grant No. 41676051) and China Scholarship Council (201906415013). We thank the China National Offshore Oil Company (CNOOC) for permission to release the data. The data that support the findings of this study are available from the CNOOC. Restrictions apply to the availability of these data, which were used under license for this study. Chief-Editor Atle Rotevatn is thanked for handling our paper. Reviewers Kamaldeen Omosanya, Isabel Edmundson and Ovie Emmanuel Eruteya are thanked for their helpful comments which are greatly improved this paper.

References

Andresen, K. J. (2012). Fluid flow features in hydrocarbon plumbing systems: What do they tell us about the basin

529 evolution? *Marine Geology*, 332-334, 89-108. doi:10.1016/j.margeo.2012.07.006.

530 Anka, Z., Berndt, C., & Gay, A. (2012). Hydrocarbon leakage through focused fluid flow systems in continental
531 margins Preface. *Marine Geology*, 33-334, 1-3, doi:10.1016/j.margeo.2012.10.012.

532 Aydin, A. (2000). Fractures, faults, and hydrocarbon entrapment, migration and flow. *Marine and Petroleum Geology*,
533 17, 797-814. doi:10.1016/S0264-8172(00)00020-9.

534 Baudon, C., & Cartwright, J. (2008a). Early stage evolution of growth faults: 3D seismic insights from the Levant
535 Basin, Eastern Mediterranean. *Journal of Structural Geology*, 30, 888-898. doi:10.1016/j.jsg.2008.02.019.

536 Baudon, C., & Cartwright, J. (2008b). 3D seismic characterisation of an array of blind normal faults in the Levant
537 Basin, Eastern Mediterranean. *Journal of Structural Geology*, 30, 746-760. doi: 10.1016/j.jsg.2007.12.008.

538 Berndt, C. (2005). Focused fluid flow in passive continental margins. *Philosophical Transactions of the Royal
539 Society A*, 363, 2855-2871. doi:10.1098/rsta.2005.1666.

540 Berndt, C., Bünz, S., Clayton, T., Mienert, J., & Saunders, M. (2004). Seismic character of bottom simulating
541 reflectors: examples from the mid-Norwegian margin. *Marine and Petroleum Geology*, 21, 723-733. doi:
542 10.1016/j.marpetgeo.2004.02.003.

543 Berndt, C., Costa, S., Canals, M., Camerlenghi, A., de Mol, B., & Saunders, M. (2012). Repeated slope failure linked
544 to fluid migration: The Ana submarine landslide complex, Eivissa Channel, Western Mediterranean Sea. *Earth
545 and Planetary Science Letters*, 319-320, 65-74. doi:10.1016/j.epsl.2011.11.045.

546 Bertoni C., Cartwright, J., Foschi M., & Martin, J. (2018). Spectrum of gas migration phenomena in multi-layered
547 sealing sequences. *AAPG Bulletin*, 102, 1011-1034. doi:10.1306/0810171622617210.

548 Brown, A. R. (2004). Interpretation of three-dimensional seismic data: AAPG Memoir 42, 6thed. SEG Investigations
549 in Geophysics.

550 Bünz, S., Mienert, J., & Berndt, C. (2003). Geological controls on the Storegga gas-hydrate system of the mid-

551 Norwegian continental margin. *Earth and Planetary Science Letters*, 209, 291-307. doi: 10.1016/S0012-
552 821X(03)00097-9.

553 Cartwright, J. A., Huuse, M., & Aplin, A. (2007). Seal bypass systems. *AAPG Bulletin*, 91, 1141-1166.
554 doi:10.1306/04090705181.

555 Calvès, G., Huuse, M., Schwab, A., & Clift, P. (2008). Three-dimensional seismic analysis of high-amplitude
556 anomalies in the shallow subsurface of the Northern Indus Fan: Sedimentary and/or fluid origin. *Journal of*
557 *Geophysics Research*, 113, B11103. doi:10.1029/2008JB005666.

558 Chen, D. X., Wu, S. G., Dong, D. D., Mi, L. J., Fu, S. Y., & Shi, H. S. (2013). Focused fluid flow in the Baiyun Sag,
559 northern South China Sea: Implications for the source of gas in hydrate reservoirs. *Chinese Journal of Oceanology*
560 *and Limnology*, 31, 178-189. doi:10.1007/s00343-013-2075-5.

561 Chopra, S., & Marfurt, K. J. (2007). Seismic attributes for prospect identification and reservoir characterization.
562 Society of Exploration Geophysicists (SEG), pp. 481.

563 Clifton, A. E., Schlische, R. W., Withjack, M. O., & Ackermann, R. V. (2000). Influence of rift obliquity on fault-
564 population systematics: results of experimental clay models. *Journal of Structural Geology*, 22, 1491-1509.
565 doi:10.1016/S0191-8141(00)00043-2.

566 Cowley, R., & O'Brien, G.W. (2000). Identification and interpretation of leaking hydrocarbons using seismic data: a
567 comparative montage of examples from the major fields in Australia's Northwest shelf and Gippsland Basin.
568 *APPEA Journal*, 40, 121-150. doi:

569 Dahlberg E. C. (1995). Applied hydrodynamics in petroleum exploration, 2nd Edition, New York: Springer - Verlag.
570 pp. 295.

571 Deng, P., Mei, L.F., Liu, J., Zheng, J. Y., Liu, M. H., Cheng, Z. J., & Guo, F. T. (2019). Episodic normal faulting and
572 magmatism during the syn-spreading stage of the Baiyun sag in Pearl River Mouth Basin: Response to the multi-

573 phase seafloor spreading of the South China Sea. *Marine Geophysical Research*, 40, 33-50. doi:10.1007/s11001-
574 018-9352-9.

575 Dong, D. D., Zhang, G. C., Zhong, K., Yuan, S. Q., & Wu, S. G. (2009). Tectonic evolution and dynamics of
576 deepwater area of Pearl River Mouth Basin, northern South China Sea. *Journal of Earth Sciences*, 20, 147-159.
577 doi:10.1007/s12583-009-0016-1.

578 Edmundson, I., Rotevatn, A., Davies, R., Yielding, G., & Broberg, K. (2019). Key controls on hydrocarbon retention
579 and leakage from structural traps in the Hammerfest Basin, SW Barents Sea: implications for prospect analysis
580 and risk assessment. *Petroleum Geoscience*, in press. doi: 10.1144/petgeo2019-094.

581 Eruteya, O. E., Reshef, M., Ben-Avraham, Z., & Waldmann, N. (2018). Gas escape along the Palmachim disturbance
582 in the Levant Basin, offshore Israel. *Marine and Petroleum Geology*, 926, 868-879. doi:
583 10.1016/j.marpetgeo.2018.01.007.

584 Eruteya, O. E., Waldmann, N., Schalev, D., Makovsky, Y., & Ben-Avraham, Z. (2015). Intra-to post-Messinian deep-
585 water gas piping in the Levant Basin, SE Mediterranean. *Marine and Petroleum Geology*, 66, 246-261.
586 doi:10.1016/j.marpetgeo.2015.03.007.

587 Feng, D., Cheng, M., Kiel, S., Qiu, J. W., Yang, Q. H., Zhou, H. Y., Peng, Y. B., & Chen, D. F. (2015). Using
588 Bathymodiolus tissue stable carbon, nitrogen and sulfur isotopes to infer biogeochemical process at a cold seep
589 in the South China Sea. *Deep Sea Research Part I: Oceanographic Research Papers*, 104, 52-59.
590 doi:10.1016/j.dsr.2015.06.011.

591 Foschi, M., & Cartwright, J. A. (2020). Seal assessment of a major gas field via integration of seal properties and
592 leakage phenomena. *AAPG Bulletin*, 104, 1627-1648. doi: 10.1306/02282018111.

593 Foschi, M., Cartwright, J. A., & MacMinn, C. M. (2019). Sequential vertical gas charge into multilayered sequences
594 controlled by central conduits. *AAPG Bulletin*, 102, 855-883. doi:10.1016/10.1306/07111717004.

595 Foschi, M., Cartwright, J. A., & Peel, F. J. (2014). Vertical anomaly clusters: Evidence for vertical gas migration
596 across multilayered sealing sequences. *AAPG Bulletin*, 98, 1859-1884. doi:10.1306/04051413121.

597 Gay, A., Lopez, M., Berndt, C., & Séranne, M. (2007). Geological controls on focused fluid flow associated with
598 seafloor seeps in the Lower Congo Basin. *Marine Geology*, 244, 68-92. doi:10.1016/j.margeo.2007.06.003.

599 Gong, Z. S., & Li, S. T. (1997). Continental margin basin analysis and hydrocarbon accumulation of the northern
600 South China Sea. Science Press, Beijing, pp. 1-510.

601 Gong, Z. S., & Li, S. T. (2004). Active heat fluid, oil and gas pool-forming dynamics in north marginal basins of
602 South China Sea. Science Press, Beijing, pp. 1-326.

603 Haq, B.U., Hardenbol, J., Vail, P.R., 1987. Chronology of fluctuating sea-levels since the Triassic. *Science*, 235:
604 1156–1167.

605 Heggland, R. (1997). Detection of gas migration from a deep source by the use of exploration 3D seismic data.
606 *Marine Geology*, 137, 41-47. doi:10.1016/S0025-3227(96)00077-1.

607 Heggland, R. (2014). Visualization and Interpretation of Gas Chimneys in Exploration for Hydrocarbons. EAGE
608 Shallow Anomalies Workshop - Indications of prospective petroleum systems? Malta, doi:10.3997/2214-
609 4609.20147430.

610 Heggland, R. (2004). Definition of geohazards in exploration 3-D seismic data using attributes and neural-network
611 analysis. *AAPG Bulletin*, 88, 857-868. doi:10.1306/02040404019.

612 He, J. X., Chen, S. H., Liu, H. L., & Liu, S. L. (2009). Natural gas genetic types and source rocks in the northern
613 slope of Baiyun Sag to Panyu Low Uplift in Pearl River Mouth Basin. *Acta Petrolei Sinica*, 30, 16-21 (in Chinese
614 with English Abstract).

615 He, M., Zhuo, H. T., Chen, W. T., Wang, Y. M., Du, J. Y., Liu, L. H., Wang, L. L., & Wan, H. Q. (2017). Sequence
616 stratigraphy and depositional architecture of the Pearl River Delta system, northern South China Sea: An

617 interactive response to sea level, tectonics and paleoceanography. *Marine and Petroleum Geology*, 84, 76-101.
618 doi:10.1016/j.marpetgeo.2017.03.022.

619 Ho, S., Cartwright, J. A., & Imbert, P. (2012). Vertical evolution of fluid venting structures in relation to gas flux, in
620 the Neogene-Quaternary of the Lower Congo Basin, Offshore Angola. *Marine Geology*, 332-334, 40-55.
621 doi:10.1016/j.margeo.2012.08.011.

622 Hovland, M., Croker, P. F., & Martin, M. (1994). Fault-associated seabed mounds (carbonate knolls?) off western
623 Ireland and north-west Australia. *Marine and Petroleum Geology*, 11, 232-246. doi:10.1016/0264-
624 8172(94)90099-X.

625 Huang, B., Xiao, X., & Zhang, M. (2003). Geochemistry, grouping and origins of crude oils in the Western Pearl
626 River Mouth Basin, offshore South China Sea. *Organic Geochemistry*, 34, 993-1008. doi:10.1016/S0146-
627 6380(03)00035-4.

628 Hubbert M. K. (1953). Entrapment of petroleum under hydrodynamic condition. *AAPG Bulletin*, 37, 1954-2026.

629 Jackson, C. A. L., & Rotevatn, A. (2013). 3D seismic analysis of the structure and evolution of a salt-influenced
630 normal fault zone: a test of competing fault growth models. *Journal of Structural Geology*, 54, 215.
631 doi:10.1016/j.jsg.2013.06.012.

632 Jourde, H., Flodin, E. A., Aydin, A., Durlofsky, L. J., & Wen, X. H. (2002). Computing permeability of fault zones
633 in eolian sandstone from outcrop measurements. *AAPG Bulletin*, 86, 1187-1200. doi:10.1306/61EEDC4C-173E-
634 11D7-8645000102C1865D.

635 Judd, A. G., & Hovland, M. (2007). Seabed Fluid Flow: The Impact on Geology, Biology and the Marine
636 Environment. Cambridge University Press, Cambridge, pp. 163-178.

637 Karfurt, K. J., & Alves, T. M. (2015). Pitfalls and limitations in seismic attribute interpretation of tectonic features.
638 *Interpretation*, 3, SB5-SB15. doi: 10.1190/INT-2014-0122.1.

639 Karstens, J., & Berndt, C. (2015). Seismic chimneys in the Southern Viking Graben - Implications for palaeo fluid
640 migration and overpressure evolution. *Earth and Planetary Science Letters*, 412, 88-100.
641 doi:10.1016/j.epsl.2014.12.017.

642 Lefèvre, M., Guglielmi, Y., Henry, P., Dick, P., & Gout, C. (2016). Calcite veins as an indicator of fracture dilatancy
643 and connectivity during strike-slip faulting in Toarcian shale (Tournemire tunnel, Southern France). *Journal of*
644 *Structural Geology*, 83, 73-84. doi:10.1016/j.jsg.2016.01.002.

645 Ligtenberg, J. H. (2005). Detection of fluid migration pathways in seismic data: implications for fault seal analysis.
646 *Basin Research*, 17, 141-153. doi:10.1111/j.1365-2117.2005.00258.x.

647 Liu, H. L., Mei, L. F., Shi, H. S., Yu, S., Wei, T., & Qing, Y. (2018). Rift Style Controlled by Basement Attribute and
648 Regional Stress in Zhu I Depression, Pearl River Mouth Basin. *Earth Science*, 35, 1-16. doi:
649 10.3799/dqkx.2018.576.

650 Løseth, H., Gading, M., & Wensaas, L. (2009). Hydrocarbon leakage on seismic data. *Marine and Petroleum*
651 *Geology*, 26, 1304-1319. doi:10.1016/j.marpetgeo.2008.09.008.

652 Lüdmann, T., & Wong, H. K. (1999). Neotectonic regime on the passive continental margin of the northern South
653 China Sea. *Tectonophysics*, 311, 113-138. doi:10.1016/S0040-1951(99)00155-9.

654 McClay, K., & White, M. J. (1995). Analogue modeling of orthogonal and oblique rifting. *Marine and Petroleum*
655 *Geology*, 12, 137-151. doi:10.1016/0264-8172(95)92835-K.

656 Mohammedyasin, S. M., Lippard, S. J., Omosanya, K. O., Johansen, S. E., & Harishidayat, D. (2016). Deep-seated
657 faults and hydrocarbon leakage in the Snøhvit Gas Field, Hammerfest Basin, Southwestern Barents Sea. *Marine*
658 *and Petroleum Geology*, 77, 160-178. doi: 10.1016/j.marpetgeo.2016.06.011.

659 Moss, J. L., & Cartwright, J. (2010). 3D seismic expression of km-scale fluid escape pipes from offshore Namibia.
660 *Basin Research*, 22, 481-501. doi:10.1111/j.1365-2117.2010.00461.x.

661 Mourgues, R., & Cobbold, P. R. (2003). Some tectonic consequences of fluid overpressures and seepage forces as
662 demonstrated by sandbox modeling. *Tectonophysics*, 376, 75-97. doi:10.1016/S0040-1951(03)00348-2.

663 Muraoka, H., & Kamata, H. (1983). Displacement distribution along minor fault traces. *Journal of Structural*
664 *Geology*, 5, 483-495. doi:10.1016/0191-8141(83)90054-8.

665 O'Brien, G. W., & Woods, E. P. (1995). Hydrocarbon-related diagenetic zones (HRDZs) in the Vulcan Sub-basin,
666 Timor Sea: recognition and exploration implications. *APEA Journal*, 35, 220-252.

667 Omosanya, K. O., Johansen, S. E., & Harishidayat, D. (2015). Evolution and character of supra-salt faults in the
668 Easternmost Hammerfest Basin, SW Barents Sea. *Marine and Petroleum Geology*, 66, 1013-1028. doi:
669 10.1016/j.marpetgeo.2015.08.010.

670 Ostanin, I., Anka, Z., & di Primio, R. (2017). Role of faults in hydrocarbon leakage in the Hammerfest Basin, SW
671 Barents Sea: Insights from seismic data and numerical modelling. *Geosciences*, 7, 28.
672 doi:10.3390/geosciences7020028.

673 Ostanin, I., Anka, Z., di Primio, R., & Bernal, A. (2013). Hydrocarbon plumbing systems above the Snøhvit gas
674 field: Structural control and implications for thermogenic methane leakage in the Hammerfest Basin, SW Barents
675 Sea, *Marine and Petroleum Geology*, 43, 127-146. doi: 10.1016/j.marpetgeo.2013.02.012.

676 Pang, X., Chen, C. M., & Peng, D. J. (2007). The pearl river deep-water fan system and petroleum in South China
677 Sea. Science Press, Beijing, pp. 38-153.

678 Pang, X., Chen, C. M., Peng, D. J., Zhou, D., Shao, L., & He, M., Liu, B. J. (2008). Basic geology of Baiyun deep-
679 water area in the northern South China Sea. *China Offshore Oil and Gas*. 20, 216-222 (in Chinese with English
680 Abstract).

681 Ping, H. W., Chen, H. H., Zhai, P. Q., Zhu, J. Z., & George, S. C. (2019). Petroleum charge history in the Baiyun
682 depression and Panyu lower uplift in the Pearl River Mouth Basin, northern South China Sea: Constraints from

683 integration of organic geochemical and fluid inclusion data. *AAPG Bulletin*, 103, 1401-1442.
684 doi:10.1306/11151817369.

685 Ping, H. W., Chen, H. H., Zhu, J. Z., George, S. C., Mi, L. J., Pang, X., & Zhai, P. Q. (2018). Origin, source, mixing,
686 and thermal maturity of natural gases in the Panyu lower uplift and the Baiyun depression, Pearl River Mouth
687 Basin, northern South China Sea. *AAPG Bulletin*, 102, 2171-2200. doi:10.1306/04121817160.

688 Roberts, H. H., & Carney, R. (1997). Evidence of episodic fluid, gas and sediment venting, northern Gulf of Mexico
689 continental slope. *Economic Geology*, 92, 863-879. doi:10.2113/gsecongeo.92.7-8.863.

690 Roberts, H. H., Sassen, R., & Milkov, A. (2000). Seafloor expression of fluid and gas expulsion from deep petroleum
691 systems, deep-water Gulf of Mexico, in Weimer, P., eds., Petroleum systems of deep-water basins: Gulf Coast
692 Section SEPM 21st Annual Research Conference, p. 401-422.

693 Ru, K., & Pigott, J. D. (1986). Episodic rifting and subsidence in the South China Sea. *AAPG Bulletin*, 70, 1136-
694 1155. doi:10.1306/94886A8D-1704-11D7-8645000102C1865D.

695 Sales, J. K. (1997). Seal strength vs. trap closure - a fundamental control on the distribution of oil and gas. In: Seals,
696 Traps, and the Petroleum System. The American Association of Petroleum Geologists AAPG, Tulsa, Oklahoma,
697 USA. AAPG Memoir, 67, 57-83.

698 Shi, H. S., Qin, C. G., Gao, P., Zhang, Z. T., Zhu, J. Z., & Zhao, R. Y. (2008). Late gas accumulation characteristics
699 in Panyu low-uplift and the north slope of Baiyun Sag, Pearl River Mouth basin. *China Offshore Oil and Gas*, 20,
700 73-76 (in Chinese with English Abstract).

701 Shi, H. S., Qin, C. G., Zhang, Z. T., Xuan, Y. H. (2009). A discussion on the complex hydrocarbon transport system
702 in the northern slope of Baiyun sag-Panyu low uplift, Pearl River Mouth basin. *China Offshore Oil and Gas*, 21,
703 361-366 (in Chinese with English Abstract).

704 Sun, Q. L., Wu, S. G., Cartwright, J., & Dong, D. D. (2012). Shallow gas and focused fluid flow systems in the Pearl

705 River Mouth Basin, northern South China Sea. *Marine Geology*, 315-318, 1-14.
 706 doi:10.1016/j.margeo.2012.05.003.

707 Sun, Q. L., Wu, S. G., Hovland, M., Luo, P., Lu, Y. T., & Qu, T. L. (2011). The morphologies and genesis of mega-
 708 pockmarks near the Xisha Uplift, South China Sea. *Marine and Petroleum Geology*, 28, 1146-1156.
 709 doi:10.1016/j.marpetgeo.2011.03.003.

710 Sun, Q. L., Wu, S. G., Cartwright, J., Wang, S. H., Lu, Y. T., Chen, D. X., & Dong, D. D. (2014b). Neogene igneous
 711 intrusions in the northern South China Sea: Evidence from high-resolution three dimensional seismic data. *Marine
 712 and Petroleum Geology*, 54, 83-95. doi:10.1016/j.marpetgeo.2014.02.014.

713 Sun, Z., Xu, Z. Y., Sun, L. T., Pang, X., Yan, C. Z., Li, Y. P., Zhao, Z. X., Wang, Z. F., & Zhang, C. M. (2014a). The
 714 mechanism of post-rift fault activities in Baiyun sag, Pearl River Mouth basin. *Journal of Asian Earth Sciences*,
 715 89, 76-89. doi:10.1016/j.jseaes.2014.02.018.

716 Traynor, J.J., & Sladen, C. (1997). Seepage in Vietnam - onshore and offshore examples. *Marine and Petroleum
 717 Geology*, 14, 345-362. doi:10.1016/S0264-8172(96)00040-2.

718 Tvedt, A. B., M., Rotevatn, A., Jackson, C. A. -L., Fossen, H., & Gawthorpe, R. L. (2013). Growth of normal faults
 719 in multilayer sequences: A 3D seismic case study from the Egersund Basin, Norwegian North Sea. *Journal of
 720 Structural Geology*, 55, 1-20. doi: 10.1016/j.jsg.2013.08.002.

721 Wang, B. (2007). Hydrocarbon migration pathway system of Panyu Low Uplift in the Pearl River Mouth Basin.
 722 Master Thesis, China University of Geosciences (Wuhan), pp. 1-70 (in Chinese with English Abstract).

723 Wang, Y. F., Wang, Y. M., Xu, Q., Li, D., Zhuo, H. T., & Zhou, W. (2012). The early-middle Miocene submarine fan
 724 system in the Pearl River Mouth Basin, South China Sea. *Petroleum Science*, 9, 1-9. doi:10.1007/s12182-012-
 725 0175-z.

726 Xu, S.C., Yang, S.K., Huang, L.F., 1995. The application of sequence stratigraphy to stratigraphic correlation. *Earth*

727 Science Frontiers, 2: 115-123 (in Chinese with English abstract).

728 Yielding, G., Freeman, B., & Needham, D. T. (1997). Quantitative fault seal prediction. *AAPG Bulletin*, 81, 897-917.

729 doi:10.1306/522b498d-1727-11d7-8645000102c1865d.

730 Yu, H. S. (1994). Structure, stratigraphy and basin subsidence of Tertiary basins along the Chinese southeastern

731 continental margin. *Tectonophysics*, 253, 63-76. doi:10.1016/0040-1951(94)90017-5.

732 Yu, S. M., Mei, L. F., Shi, H. S., Qin, C. G., & Tang, J. G. (2007). Relationship between faults and hydrocarbon

733 accumulation in Panyu low massif and north slope of Baiyun Sag, Pearl River Mouth Basin. *Petroleum*

734 *Exploration and Development*, 34, 562-579 (in Chinese with English Abstract).

735 Zhang, Z. T., Shi, H. S., Qin, C. G., Gao, P., & Qu, L. (2010). Study on fault sealability of Panyu Low Massif and

736 north slope of Baiyun Sag. *Fault-Block Oil & Gas Field*, 17, 24-27 (in Chinese with English Abstract).

737 Zhu, J. Z., Shi, H. S., Pang, X., Qin, C. G., & Gao, P. (2005). Natural gas origins and gas source studies of Panyu

738 Low Uplift in Pearl River Mouth Basin. *Natural Gas Geoscience*, 16, 456-459 (in Chinese with English Abstract).

739 Zhu, J. Z., Shi, H. S., Pang, X., Qin, C. G., & Gao, P. (2006). Geochemical characteristics and oil sources of

740 condensates in Panyu Low Uplift, Pearl River Mouth basin. *China Offshore Oil and Gas*, 18, 103-106 (in Chinese

741 with English Abstract).

742 Zhu, W. L., Huang, B. J., Mi, L. J., Wilkins, R. W. T., Fu, N., & Xiao, X. (2009). Geochemistry, origin, and deep-water

743 exploration potential of natural gases in the Pearl River Mouth and Qiongdongnan basins, South China Sea. *AAPG*

744 *Bulletin*, 93, 741-761. doi:10.1306/02170908099.

745

Figure Captions

Figure 1: (a) Geological setting and subdivision of the Pearl River Mouth Basin (location in inset, blue square within the South China Sea). The study area (purple square) is located in the eastern part of the Panyu Low Massif. The boundary faults are modified from Pang et al. (2007) and Sun et al. (2014a). Top left: Geological backgrounds of the South China Sea; (b) gas fields indicated in red color in the Baiyun Sag and Panyu Low Massif. The Baiyun Sag and Panyu Low Massif are separated by the north-dipping normal faults (black dashed line) (Pang et al. 2008). The main flow directions of hydrocarbon (cyan dashed lines; Pang et al., 2007; Zhang et al., 2010) and gas charged time (Ping et al., 2019) are labeled.

Figure 2: Integrated stratigraphic column of the Pearl River Mouth Basin (modified from Pang et al., 2008; Sun et al., 2014b) with lithology (L.), seismic surfaces (S), units (U), hydrocarbon system (H.S.; the presence of source rock, reservoir and seal), relative sea-level change of the Pearl River Mouth (S.L.P.; modified from Xu et al., 1995), global relative sea-level change (S.L.G.; modified from Haq et al., 1987), tectonic events and basin events. AAs: amplitude anomalies (gas-related); D.E.B.: depositional environment in the Baiyun Sag; D.E.P.: depositional environment in the Panyu Low Massif. The main stages of each tectonic episode in the Tectonic Event column are enclosed within the red dashes. L. = Low; H. = High.

Figure 3: Composite figure depicting a representative seismic section across the study area (left, see Figure 4 for line location) calibrated with a simplified lithological column and well-log response

from well N119-5-3. The seismic basement exhibits a strong hard response and separates the featureless basement facies below from the stratified sedimentary column above. A number of normal faults transect the sedimentary column from the basement top to approximately the base of Unit 4. The sedimentary column is dominated by fine grained sequences separated by a number of sand-rich intervals. These sand-rich intervals exhibit lower gamma-ray responses and represent potential carrier beds for hydrocarbon migration. DF = Depositional facies; GI = Gas indicator; GBL = Gas-bearing layer; VE. = vertical exaggeration.

Figure 4: Composite figure showing variance extracted from the 3-D seismic data (see [Figure 1](#) for map location). (a) and (b) Variance slices of 950 ms (twt). Reflection termination associated with faults are depicted as black linear features (a). The faults have been interpreted and grouped into two groups of en-echelon faults. Locations of seismic profiles used in this study are labeled (b). SCZ: seismic chaotic zone; (c) and (d) Variance slices of 1600 ms and 2400 ms (twt). The two groups of en-echelon faults (dashed white ellipses) and SCZs from (b) are superimposed on these two variance slices. These en echelon arrays are seemly linked to the deep-seated structures in the basement.

Figure 5: Root-mean square (RMS) amplitude map of 700 - 900 ms (twt) extracted from the 3-D seismic data (a) and its interpretation (b). The RMS amplitude with high values (warm color) indicates seismic amplitude anomalies interpreted as gas. Faults from [Figure 4b](#) are superimposed on this map and three zones of high RMS amplitude values are marked.

Figure 6: Seismic cross section (see Figure 4b for line location), with interpretation of main calibrated surfaces and seismic Units, showing a basement high and the related deformation (anticline) in the overlying strata. The seismic section shows two representative fluid related features, a seismic chaotic zone (SCZ-1) and a number of stacked amplitude anomalies. The westernmost portion of the stacked anomalies and the seismic chaotic zone are located directly above the basement high. VE. = vertical exaggeration.

Figure 7: Representative seismic section (a, see Figure 4b for line location) with interpretation of main surfaces (b) showing the en-echelon faults of Group II. The inclinations of these faults in the southwestern and northeastern parts are antithetic. Amplitude anomalies (AAs) are bounded by the normal faults in the southwestern part. The numbered faults are used to show the T-z plots in Fig. 10d. VE. = vertical exaggeration.

Figure 8: Representative seismic section (see Figure 4b for line location) showing a number of south and north dipping normal faults. The bright reflectivity of the indicated surfaces is related to a lithological change rather than to a change in fluid content (e.g., gas). The shallow section is free from any evidence of fluid flow features. VE. = vertical exaggeration.

Figure 9: Seismic cross section (a, see Figure 4b for line location) and its interpretation (b) showing a number of fault bounds stacked amplitude anomalies (AAs) associated with gas. The AAs are bounded between the Group II and the Panyu Fault. Escarpment of the Panyu Fault occurs at the seabed. Small-scale AAs close to the seabed along the boundary fault are also observed. VE. =

vertical exaggeration.

Figure 10: Geomorphological characteristics of normal faults in the study area. (a), (b) and (c) are strikes, dip directions and lengths of all the normal faults (excluding the Panyu Fault), respectively. (d) T-z plots of chosen faults showing in Figure 7.

Figure 11: Representative seismic sections (a - c, see Figure 4b for line location), with interpretation of main surfaces, faults, seismic chaotic zones (SCZs), and amplitude anomalies (AAs) (b - d). The SCZs are usually characterized by 'pull-up' anomalies at their upper parts. The pull-ups are located in a shallower interval with respect to the AAs and located exactly at the fault upper tip. Some minor AAs can be observed above the pull-up regions. VE. = vertical exaggeration.

Figure 12: Composite figure showing structural maps calibrated at surface T₄ (a), surface T₃ (b), and surface along the AAs highlighted on Figure 11b. Interpreted gas-water contacts (red solid line; inferred from Pang et al., (2007) and Ping et al. (2019)) are marked in (a) and seismic chaotic zone (SCZ-1) are marked in (a)-(c). Gas coverage in the shallow level is based on the distribution of AAs. Four-way closures are mainly controlled by normal faults. Purple solid line and cyan solid line in (a) are the projections of SCZ-1 in (b) and (c); SCZ-1 is located within the four-way closures controlled by normal faults (b); Normal faults are also observed to crosscut the SCZ-1 (c).

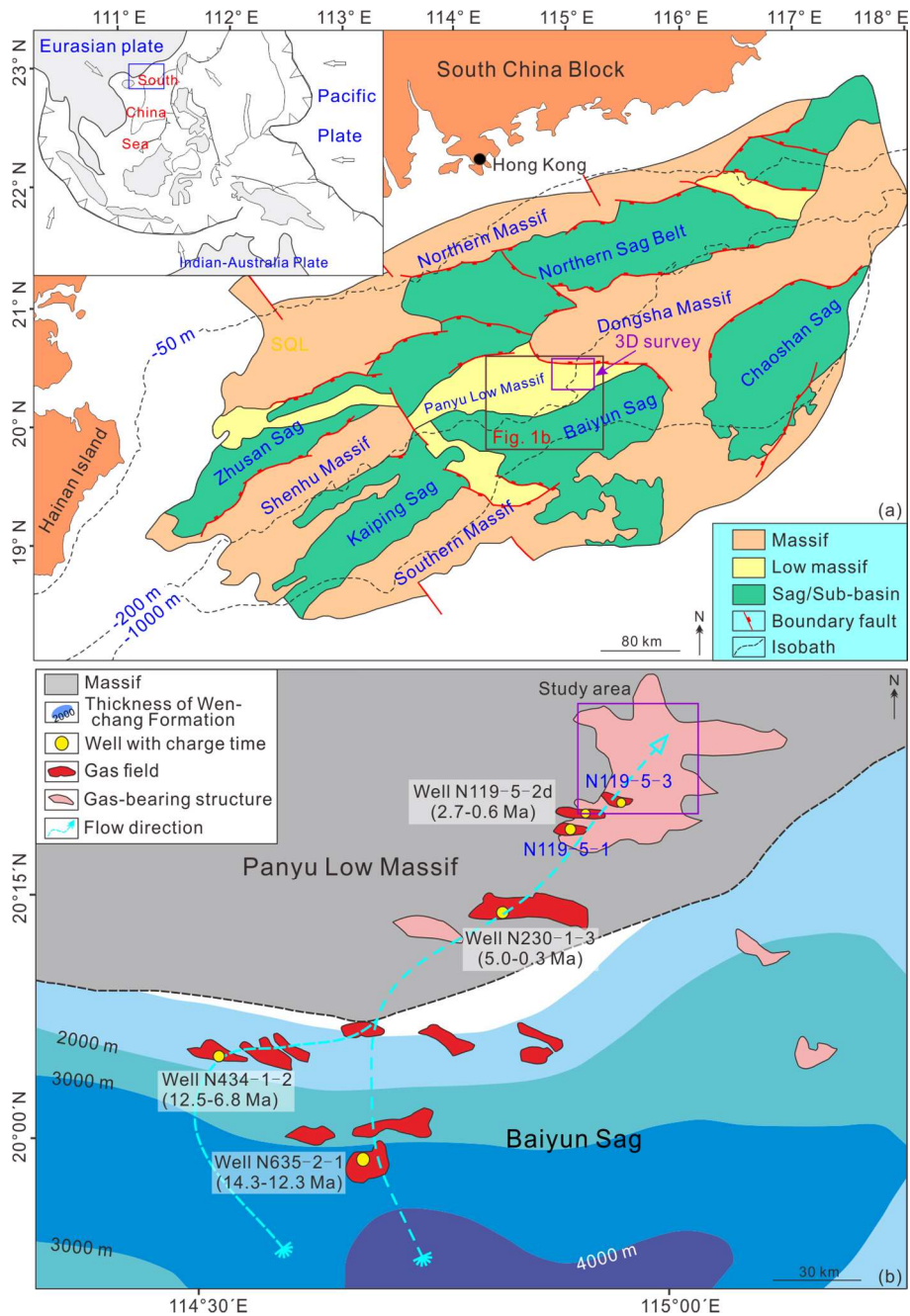
Figure 13: Time-structural map (a) and root-mean square (RMS) attribute (b) along the seabed surface. The seabed surface (a) exhibits one low-relief mounds (~10 ms TWT) occurring directly

above an amplitude anomaly (AA). The RMS attribute (b), calculated along the interval from the seabed to 30 ms TWT below, shows two AAs (bright regions) and one of them is corresponding to the mound.

Figure 14: Schematic models (a, b, and c) showing three hypothetical models for hydrocarbon migration in the study area. In the first model (a) shallow gas migrated from the Baiyun Sag through a long-distance transportation in the shallow strata with no direct vertical migration to the shallower section. In the second model (b) gas migrated from deeper to shallower sections of the basin producing a focused region as seismic chaotic zones (SCZs; e.g. gas chimneys). In the third model (c) gas migrated vertically along faults where the faults formed the four-way closures.

Figure 15: 3-D conceptual cartoon showing the hydrocarbon plumbing system active in the study area (a). In this model carrier beds at the deeper section of the basin (Units 1 and 2) allow migration along strata to the fault trap within the study area. This process occurs within those carrier beds where the fault displacement is sufficiently modest and do not completely offset the permeable pathway. The faults allow then migration across strata to the shallow level. Remigration of gas at this level (Unit 3) is observed in the form of stacked AAs. (b) 3-D conceptual cartoon showing how the gas laterally migrates through normal faults; (c) intersecting sections extracting from (b) show the relationships between lateral migrating gas and normal faults. Gas migration along strata is allowed at the tips of the en-echelon faults (i), and partly allowed where the strata is not completely offset (ii), and prevented where fault displacement is too large to allow across-fault migration (iii).

Figure 1



857

858 Figure 1: (a) Geological setting and subdivision of the Pearl River Mouth Basin (location in inset,

859 blue square within the South China Sea). The study area (purple square) is located in the eastern

860 part of the Panyu Low Massif. The boundary faults are modified from Pang et al. (2007) and Sun et

861 al. (2014a). Top left: Geological backgrounds of the South China Sea; (b) gas fields indicated in red

862 color in the Baiyun Sag and Panyu Low Massif. The main flow directions of hydrocarbon (cyan

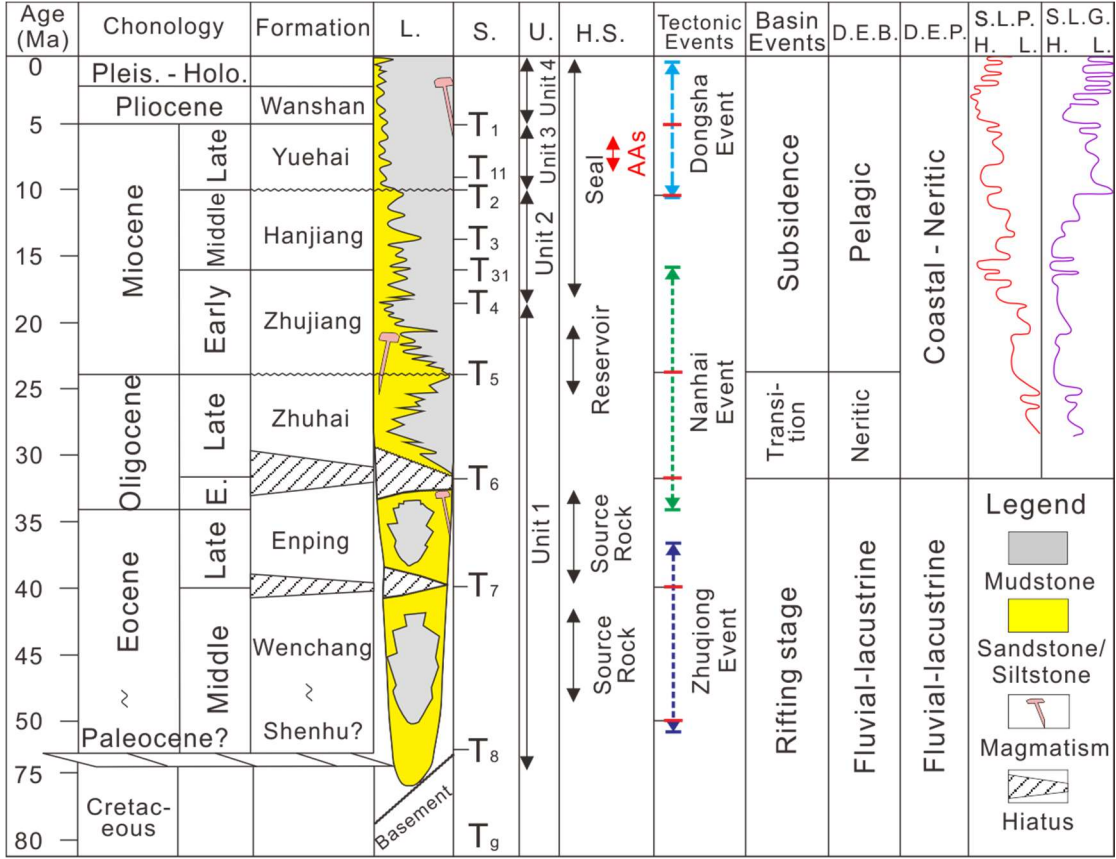
863 dashed lines; Pang et al., 2007; Zhang et al., 2010) and gas charged time (Ping et al., 2019) are

864 labeled.

865

866

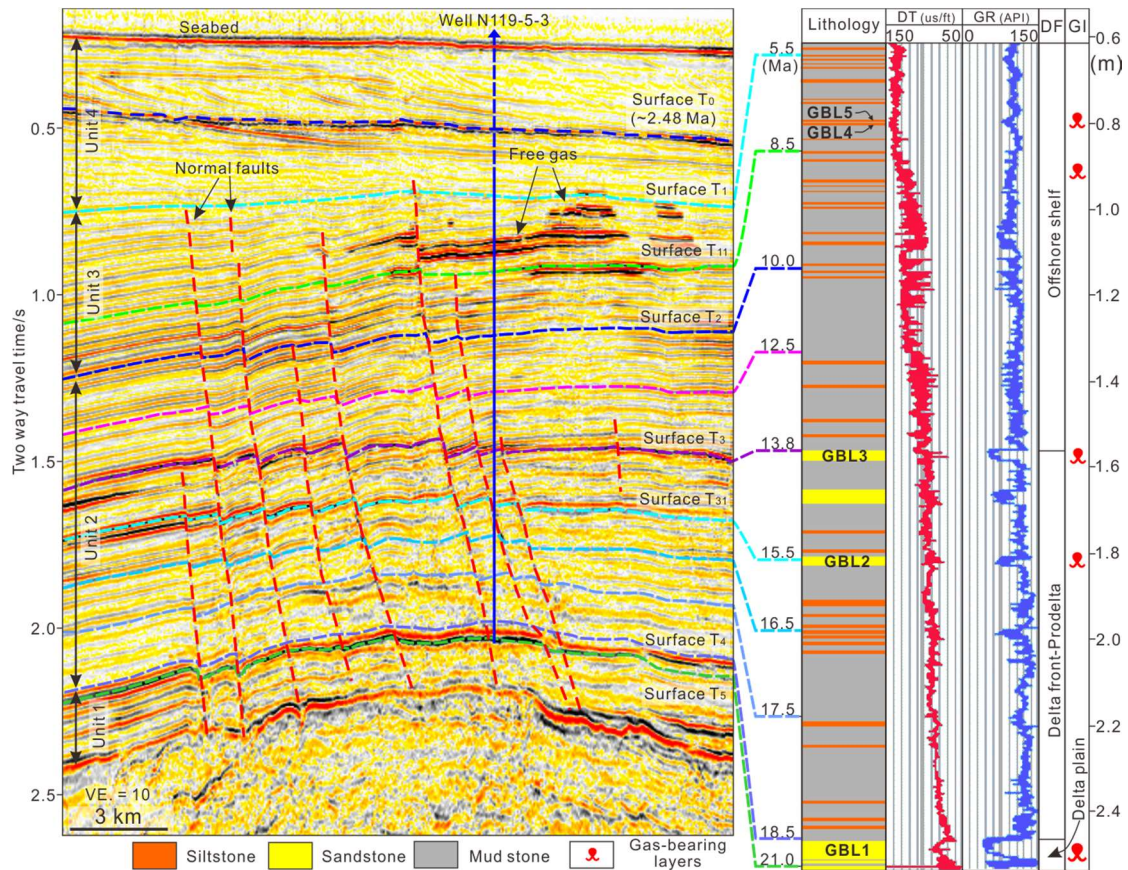
867 Figure 2



868
869 Figure 2: Integrated stratigraphic column of the Pearl River Mouth Basin (modified from Pang et
870 al., 2008; Sun et al., 2014b) with lithology (L.), seismic surfaces (S), units (U), hydrocarbon system
871 (H.S.; the presence of source rock, reservoir and seal), relative sea-level change of the Pearl River
872 Mouth (S.L.P.; modified from Xu et al., 1995), global relative sea-level change (S.L.G.; modified
873 from Haq et al., 1987), tectonic events and basin events. AAs: amplitude anomalies (gas-related);
874 D.E.B.: depositional environment in the Baiyun Sag; D.E.P.: depositional environment in the Panyu
875 Low Massif. The main stages of each tectonic episode in the Tectonic Event column are enclosed
876 within the red dashes. L. = Low; H. = High.

877

878 Figure 3



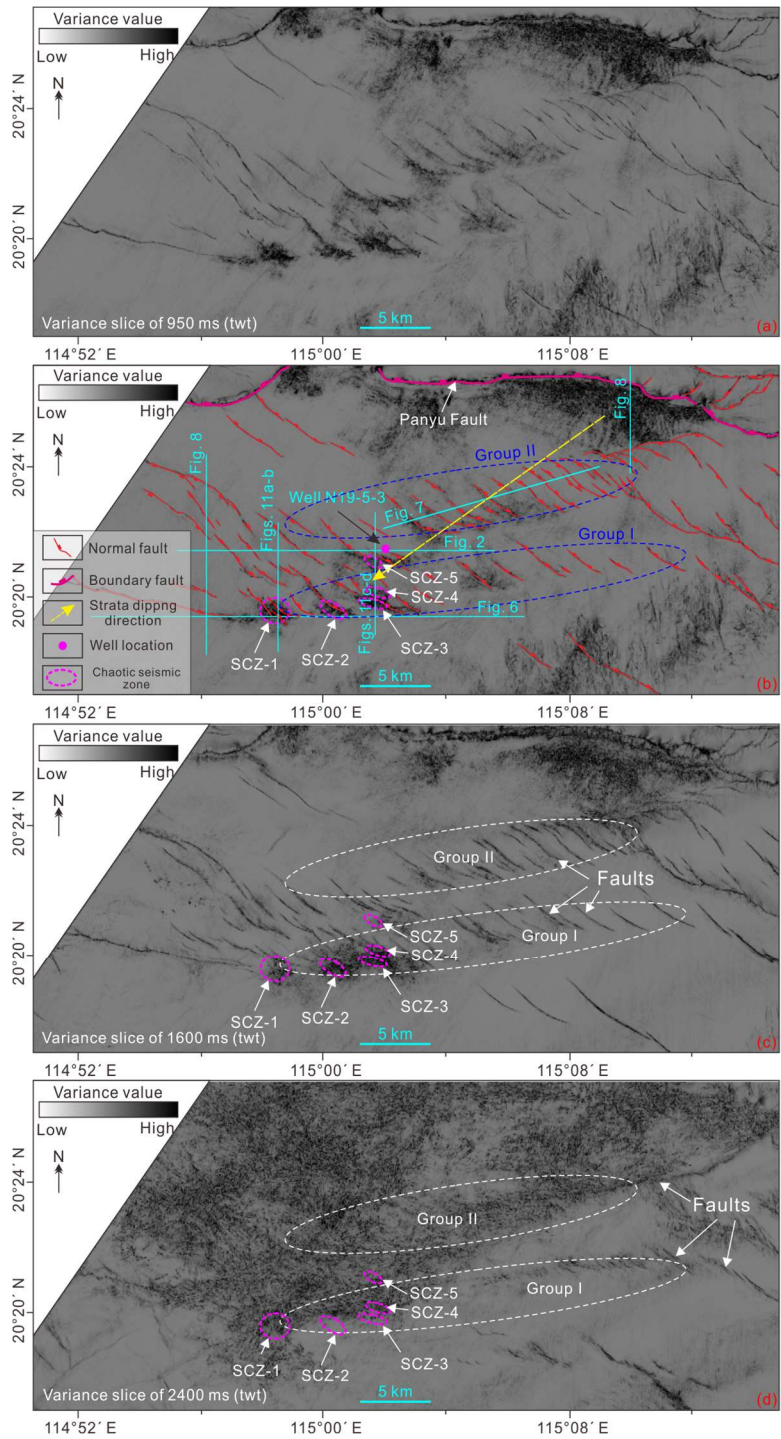
879

880

881 Figure 3: Composite figure depicting a representative seismic section across the study area (left, see
882 [Figure 4](#) for line location) calibrated with a simplified lithological column and well-log response
883 from well N119-5-3. The seismic basement exhibits a strong hard response and separates the
884 featureless basement facies below from the stratified sedimentary column above. A number of
885 normal faults transect the sedimentary column from the basement top to approximately the base of
886 Unit 4. The sedimentary column is dominated by fine grained sequences separated by a number of
887 sand-rich intervals. These sand-rich intervals exhibit lower gamma-ray responses and represent
888 potential carrier beds for hydrocarbon migration. DF = Depositional facies; GI = Gas indicator;
889 GBL = Gas-bearing layer; VE. = vertical exaggeration.

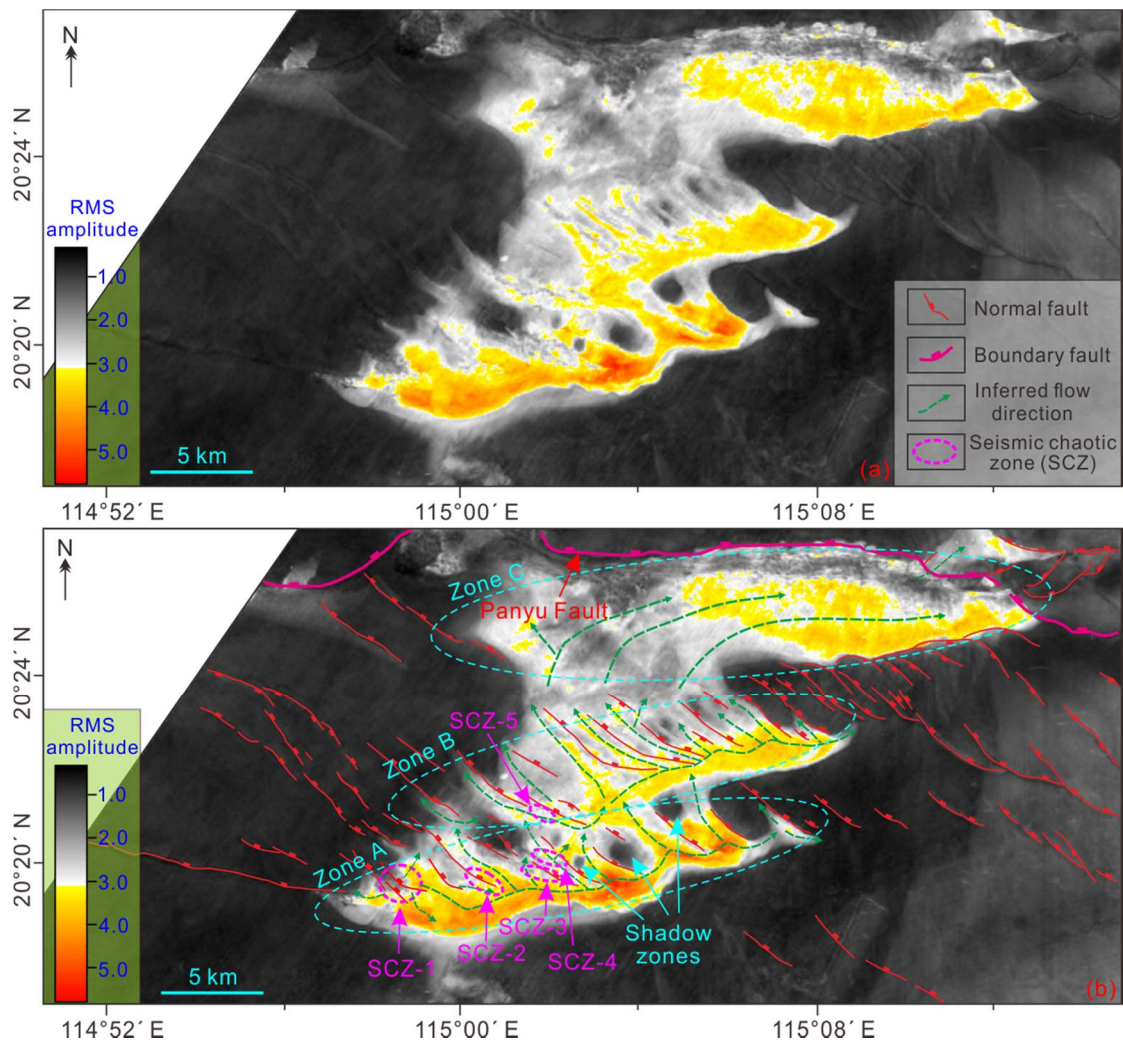
890

891 Figure 4



892
893 Figure 4: Composite figure showing variance extracted from the 3-D seismic data (see Figure 1 for
894 map location). (a) and (b) Variance slices of 950 ms (tw). Reflection termination associated with
895 faults are depicted as black linear features (a). The faults have been interpreted and grouped into
896 two groups of en-echelon faults. Locations of seismic profiles used in this study are labeled (b).
897 SCZ: seismic chaotic zone; (c) and (d) Variance slices of 1600 ms and 2400 ms (tw). The two
898 groups of en-echelon faults (dashed white ellipses) and SCZs from (b) are superimposed on them.

899 Figure 5



900
901 Figure 5: Root-mean square (RMS) amplitude map of 700 - 900 ms (twt) extracted from the 3-D
902 seismic data (a) and its interpretation (b). The RMS amplitude with high values (warm color)
903 indicates seismic amplitude anomalies interpreted as gas. Faults from Figure 4b are superimposed
904 on this map and three zones of high RMS amplitude values are marked.
905

Figure 6

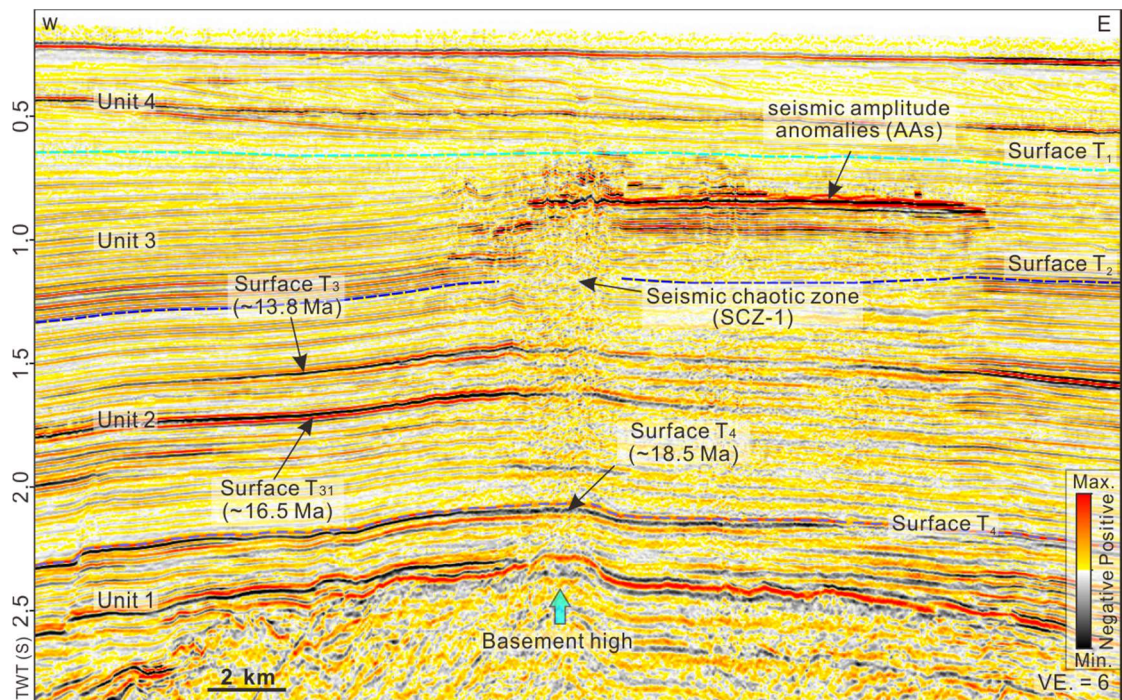
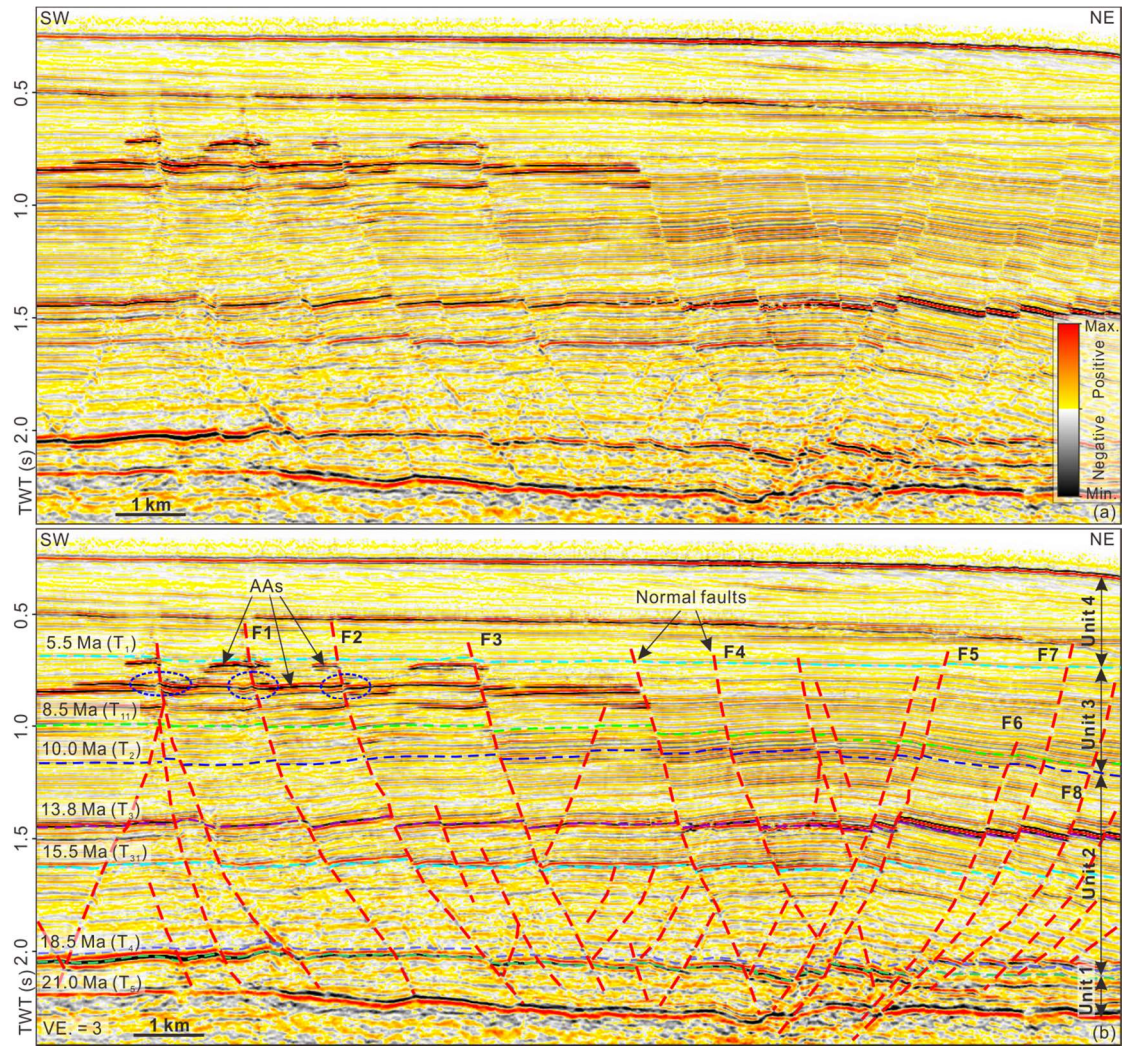


Figure 6: Seismic cross section (see Figure 4b for line location), with interpretation of main calibrated surfaces and seismic Units, showing a basement high and the related deformation (anticline) in the overlying strata. The seismic section shows two representative fluid related features, a seismic chaotic zone (SCZ-1) and a number of stacked amplitude anomalies. The westernmost portion of the stacked anomalies and the seismic chaotic zone are located directly above the basement high. VE. = vertical exaggeration.

915 Figure 7

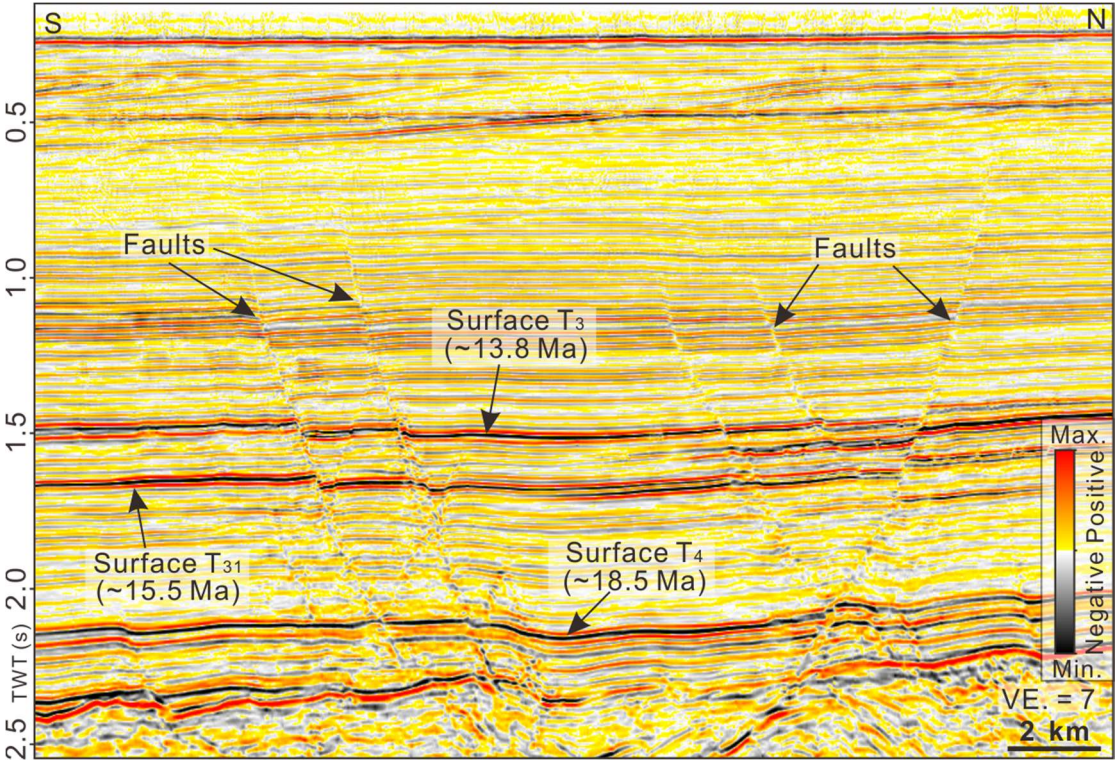


916
917

918 Figure 7: Representative seismic section (a, see Figure 4b for line location) with interpretation of
919 main surfaces (b) showing the en-echelon faults of Group II. The inclinations of these faults in the
920 southwestern and northeastern parts are antithetic. Amplitude anomalies (AAs) are bounded by the
921 normal faults in the southwestern part. The numbered faults are used to show the T-z plots in Fig.
922 10d. VE. = vertical exaggeration.

923

924 Figure 8



925

926

927 Figure 8: Representative seismic section (see Figure 4b for line location) showing a number of south
928 and north dipping normal faults. The bright reflectivity of the indicated surfaces is related to a
929 lithological change rather than to a change in fluid content (e.g., gas). The shallow section is free
930 from any evidence of fluid flow features. VE. = vertical exaggeration.

931

Figure 9

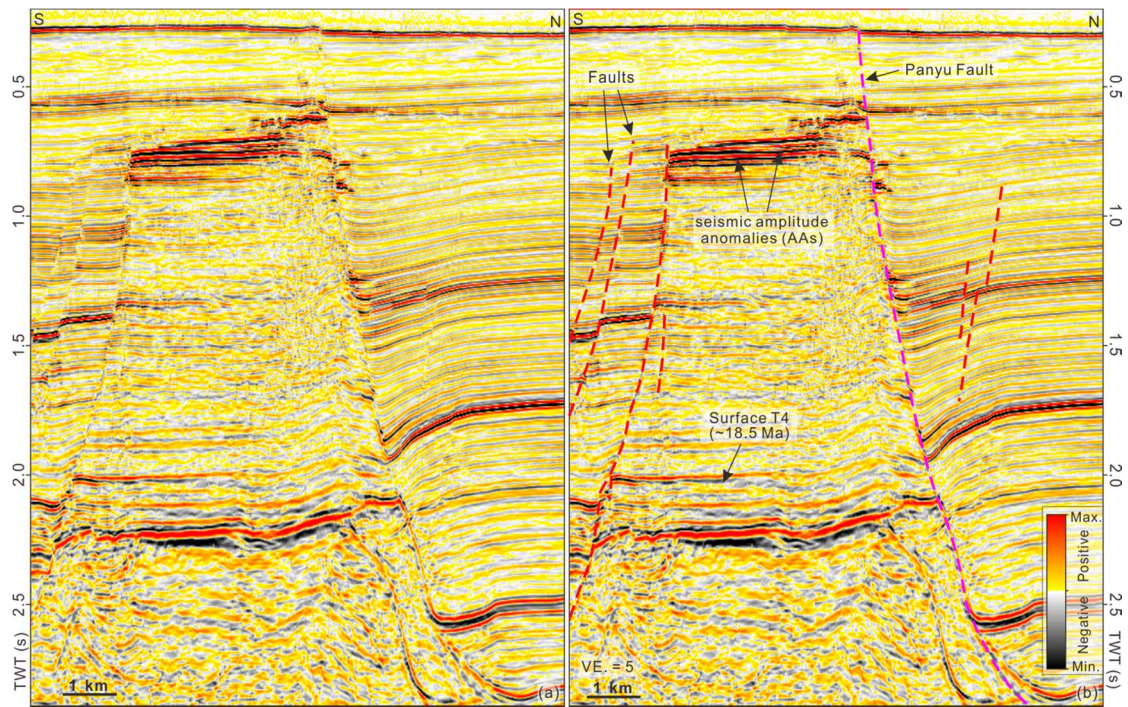
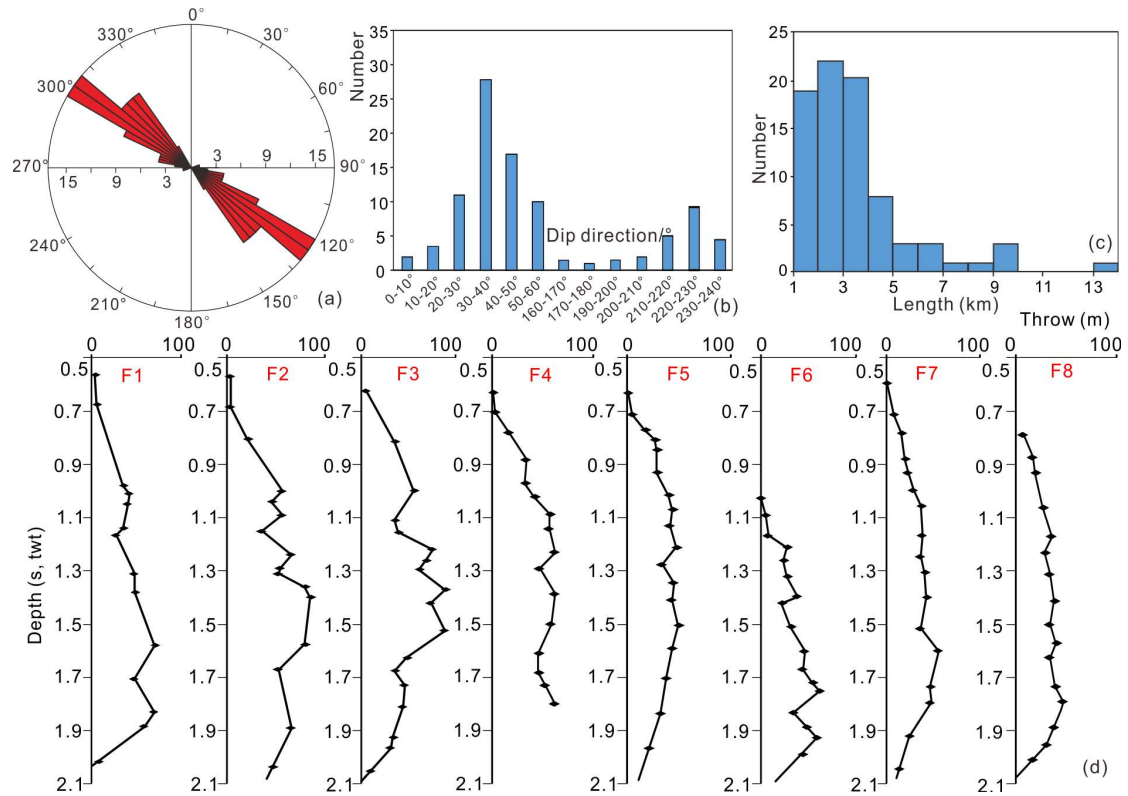


Figure 9: Seismic cross section (a, see Figure 4b for line location) and its interpretation (b) showing a number of fault bounds stacked amplitude anomalies (AAs) associated with gas. The AAs are bounded between the Group II and the Panyu Fault. Escarpment of the Panyu Fault occurs at the seabed. Small-scale AAs close to the seabed along the boundary fault are also observed. VE. = vertical exaggeration.

941 Figure 10



942
943 Figure 10: Geomorphological characteristics of normal faults in the study area. (a), (b) and (c) are
944 strikes, dip directions and lengths of all the normal faults (excluding the Panyu Fault), respectively.
945 (d) T-z plots of chosen faults showing in Figure 7.

946
947
948

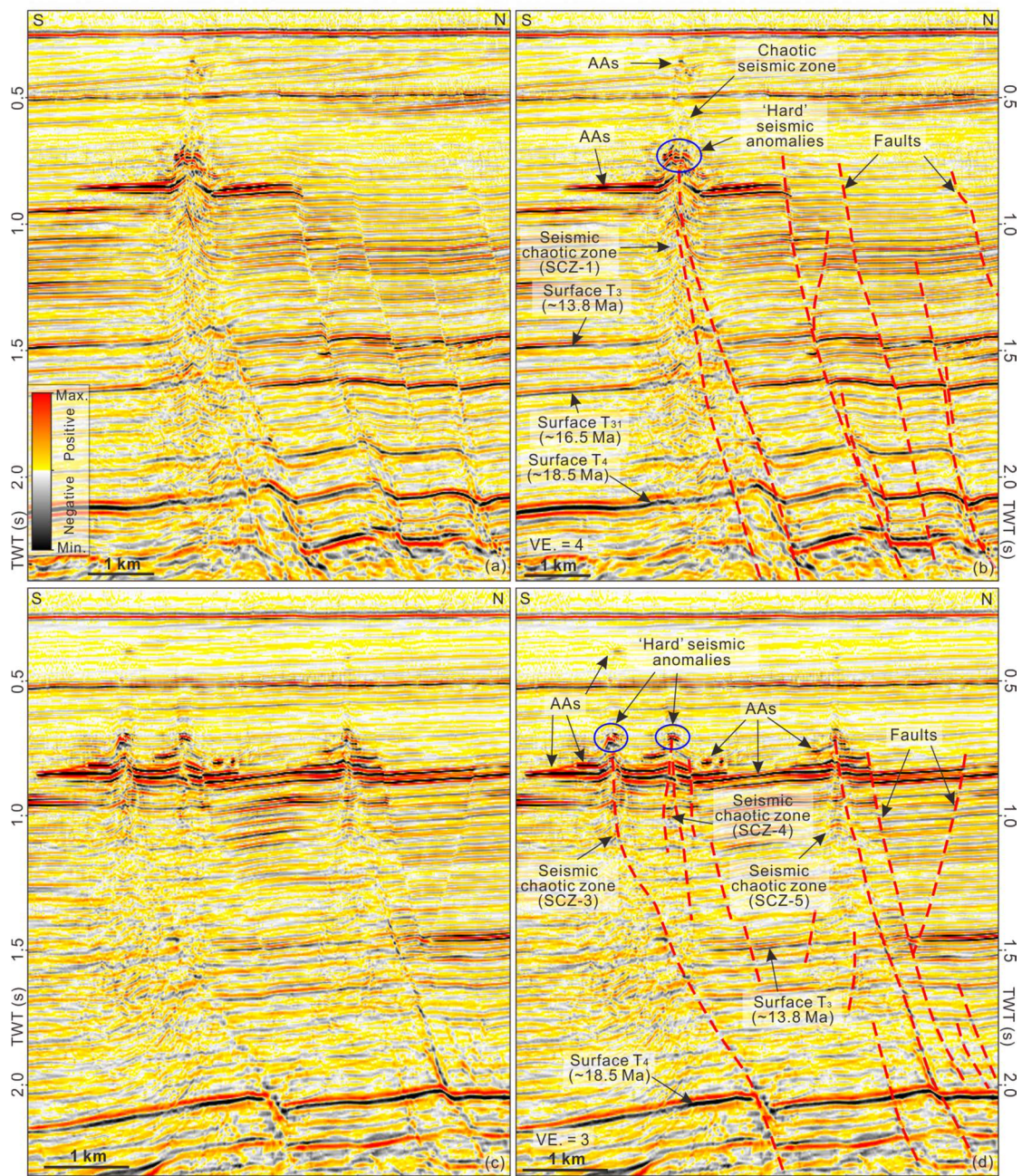
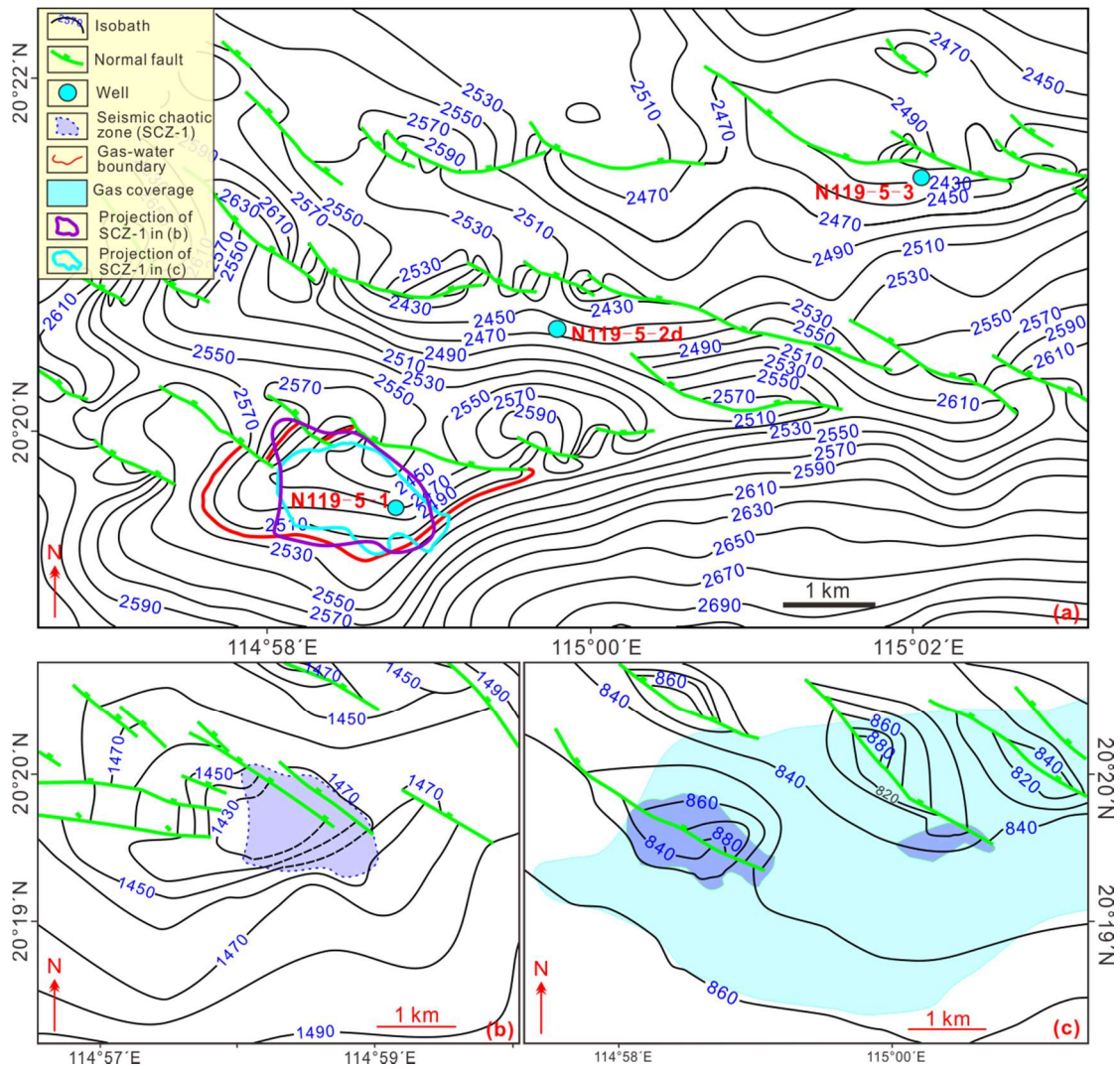


Figure 11: Representative seismic sections (a - c, see Figure 4b for line location), with interpretation of main surfaces, faults, seismic chaotic zones (SCZs), and amplitude anomalies (AAs) (b - d). The SCZs are usually characterized by ‘pull-up’ anomalies at their upper parts. The pull-ups are located in a shallower interval with respect to the AAs and located exactly at the fault upper tip. Some minor AAs can be observed above the pull-up regions. VE. = vertical exaggeration.



960

961

962 Figure 12: Composite figure showing structural maps calibrated at surface T_4 (a), surface T_3 (b),
963 and surface along the AAs highlighted on Figure 11b. Interpreted gas-water contacts (red solid
964 line; inferred from Pang et al., (2007) and Ping et al. (2019)) are marked in (a) and seismic chaotic
965 zone (SCZ-1) are marked in (a)-(c). Gas coverage in the shallow level is based on the distribution
966 of AAs. Four-way closures are mainly controlled by normal faults. Purple solid line and cyan solid
967 line in (a) are the projections of SCZ-1 in (b) and (c); SCZ-1 is located within the four-way
968 closures controlled by normal faults (b); Normal faults are also observed to crosscut the SCZ-1
969 (c).

Figure 13

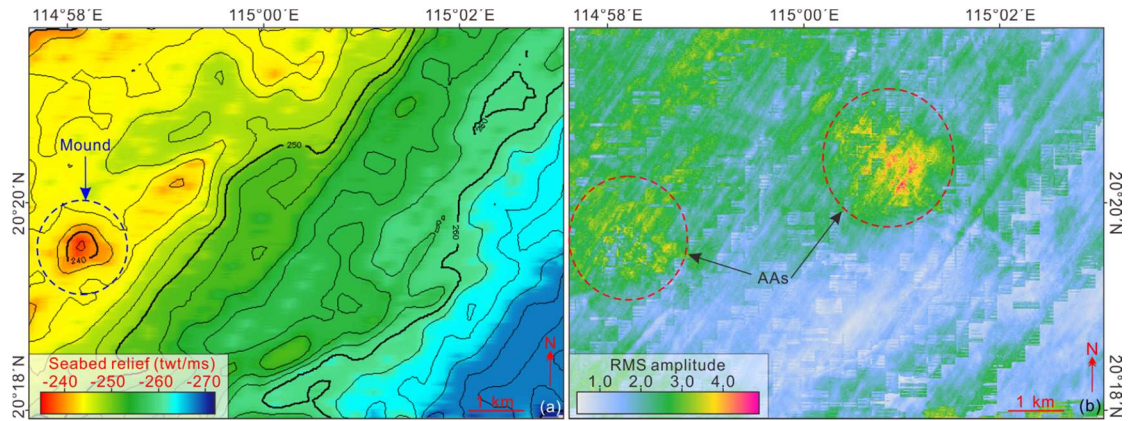


Figure 13: Time-structural map (a) and root-mean square (RMS) attribute (b) along the seabed surface. The seabed surface (a) exhibits one low-relief mounds (~10 ms TWT) occurring directly above an amplitude anomaly (AA). The RMS attribute (b), calculated along the interval from the seabed to 30 ms TWT below, shows two AAs (bright regions) and one of them is corresponding to the mound.

Figure 14

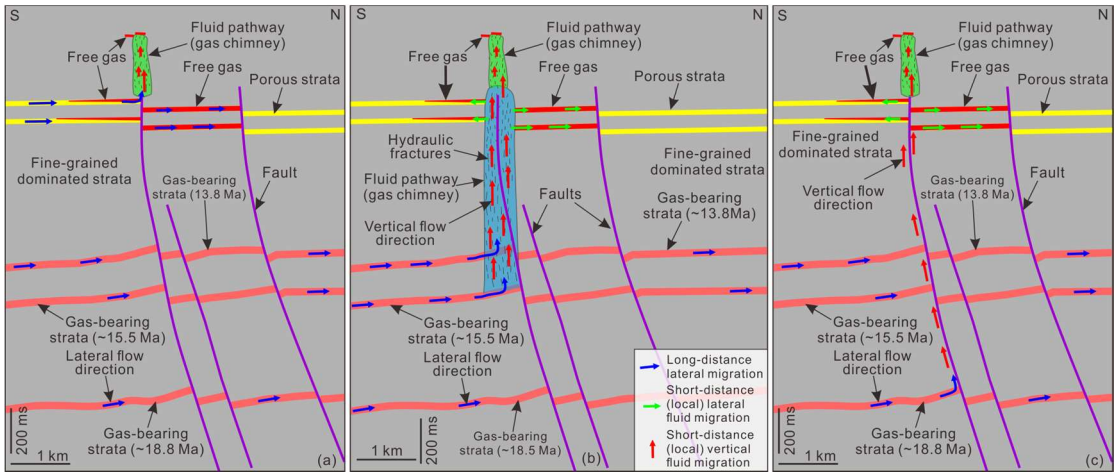


Figure 14: Schematic models (a, b, and c) showing three hypothetical models for hydrocarbon migration in the study area. In the first model (a) shallow gas migrated from the Baiyun Sag through a long-distance transportation in the shallow strata with no direct vertical migration to the shallower section. In the second model (b) gas migrated from deeper to shallower sections of the basin producing a focused region as seismic chaotic zones (SCZs; e.g. gas chimneys). In the third model (c) gas migrated vertically along faults where the faults formed the four-way closures.

